















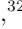

















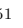






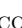




Multiwavelength Investigation of γ -ray Source MGRO J1908+06 Emission Using *Fermi*-LAT, VERITAS, and HAWC

THE VERITAS COLLABORATION

A. ACHARYYA ¹, C. B. ADAMS ², P. BANGALE ³, J. T. BARTOSKE ⁴, W. BENBOW ⁵, J. H. BUCKLEY ⁶, J. L. CHRISTIANSEN,⁷ A. J. CHROMEY,⁵ A. DUERR ⁴, M. ERRANDO ⁶, A. FALCONE ⁸, Q. FENG ⁴, G. M. FOOTE ³, L. FORTSON ⁹, A. FURNISS ¹⁰, W. HANLON ⁵, D. HANNA ¹¹, O. HERVET ¹², C. E. HINRICHS ¹³, J. HOLDER ³, T. B. HUMENSKY ¹⁴, W. JIN ¹⁵, P. KAARET ¹⁶, M. KERTZMAN,¹⁷ D. KIEDA ⁴, T. K. KLEINER ¹⁸, N. KORZOUN ³, S. KUMAR ¹⁹, M. J. LANG ²⁰, M. LUNDY ¹¹, G. MAIER ¹⁸, C. E. McGRATH,²¹ M. J. MILLARD ¹⁶, J. MILLIS,²² C. L. MOONEY ³, P. MORIARTY ²⁰, R. MUKHERJEE ²³, W. NING ¹⁵, R. A. ONG ¹⁵, N. PARK,²⁴ M. POHL ²⁵, E. PUESCHEL ²⁶, J. QUINN ²¹, P. L. RABINOWITZ,⁶ K. RAGAN ¹¹, D. RIBEIRO ⁹, E. ROACHE,⁵ J. L. RYAN ¹⁵, I. SADEH ¹⁸, L. SAHA ⁵, G. H. SEMBROSKI,²⁷ R. SHANG ²³, M. SPLETTSTOESSER ¹², A. K. TALLURI,⁹ J. V. TUCCI,²⁸ J. VALVERDE ²⁹, V. V. VASSILIEV,¹⁵ A. WEINSTEIN,³⁰ D. A. WILLIAMS ¹², S. L. WONG ¹¹, J. WOO ³¹

THE HAWC COLLABORATION

R. ALFARO ³², C. ALVAREZ,³³ J.C. ARTEAGA-VELÁZQUEZ,³⁴ D. AVILA ROJAS,³² R. BABU,³⁵ E. BELMONT-MORENO ³², A. BERNAL,³⁶ K.S. CABALLERO-MORA,³³ T. CAPISTRÁN ³⁶, A. CARRAMIÑANA ³⁷, S. CASANOVA ³⁸, J. COTZOMI ³⁹, S. COUTIÑO DE LEÓN ⁴⁰, E. DE LA FUENTE ⁴¹, D. DEPAOLI,⁴² N. DI LALLA,⁴³ R. DIAZ HERNANDEZ,³⁷ M.A. DUVERNOIS ⁴⁰, C. ESPINOZA ³², K.L. FAN,¹⁹ K. FANG ⁴⁰, N. FRAJLA ³⁶, J.A. GARCÍA-GONZÁLEZ ⁴⁴, F. GARFIAS ³⁶, M.M. GONZÁLEZ ³⁶, J.A. GOODMAN ¹⁹, S. GROETSCH,³⁵ S. HERNÁNDEZ-CADENA,³² J. HINTON,⁴² D. HUANG ¹⁹, F. HUEYOTL-ZAHUANTITLA ³³, A. IRIARTE ³⁶, S. KAUFMANN,⁴⁵ D. KIEDA,⁴⁶ J. LEE ⁴⁷, H. LEÓN VARGAS ³², A.L. LONGINOTTI ³⁶, G. LUIS-RAYA ⁴⁵, K. MALONE ⁴⁸, J. MARTÍNEZ-CASTRO ⁴⁹, J.A. MATTHEWS ⁵⁰, P. MIRANDA-ROMAGNOLI,⁵¹ J.A. MORALES-SOTO ³⁴, E. MORENO ³⁹, M. MOSTAFÁ ⁵², L. NELLEN ⁵³, E.G. PÉREZ-PÉREZ ⁴⁵, C.D. RHO ⁴⁷, D. ROSA-GONZÁLEZ ³⁷, H. SALAZAR,³⁹ A. SANDOVAL,³² M. SCHNEIDER ¹⁹, J. SERNA-FRANCO,³² Y. SON,⁴⁷ R.W. SPRINGER ⁴⁶, O. TIBOLLA,⁴⁵ K. TOLLEFSON ⁵⁴, I. TORRES ³⁷, R. TORRES-ESCOBEDO,⁵⁵ R. TURNER,³⁵ F. UREÑA-MENA,³⁷ E. VARELA,³⁹ X. WANG,³⁵ H. ZHOU ⁵⁵

THE *Fermi*-LAT COLLABORATION

J. EAGLE ⁵⁶, S. KUMAR,⁵⁷

¹*CP3-Origins, University of Southern Denmark, Campusvej 55, 5230 Odense M, Denmark*

²*Physics Department, Columbia University, New York, NY 10027, USA*

³*Department of Physics and Astronomy and the Bartol Research Institute, University of Delaware, Newark, DE 19716, USA*

⁴*Department of Physics and Astronomy, University of Utah, Salt Lake City, UT 84112, USA*

⁵*Center for Astrophysics | Harvard & Smithsonian, Cambridge, MA 02138, USA*

⁶*Department of Physics, Washington University, St. Louis, MO 63130, USA*

⁷*Physics Department, California Polytechnic State University, San Luis Obispo, CA 94307, USA*

⁸*Department of Astronomy and Astrophysics, 525 Davey Lab, Pennsylvania State University, University Park, PA 16802, USA*

⁹*School of Physics and Astronomy, University of Minnesota, Minneapolis, MN 55455, USA*

¹⁰*Department of Physics, California State University - East Bay, Hayward, CA 94542, USA*

¹¹*Physics Department, McGill University, Montreal, QC H3A 2T8, Canada*

¹²*Santa Cruz Institute for Particle Physics and Department of Physics, University of California, Santa Cruz, CA 95064, USA*

¹³*Center for Astrophysics | Harvard & Smithsonian, Cambridge, MA 02138, USA and Department of Physics and Astronomy, Dartmouth College, 6127 Wilder Laboratory, Hanover, NH 03755 USA*

Corresponding author: Ruo-Yu Shang
r.y.shang@gmail.com

Corresponding author: Jordan Eagle
jordan.l.eagle@nasa.gov

Corresponding author: Sajjan Kumar
sajkumar@udel.edu

Corresponding author: S. Coutiño De León
scoutino@icecube.wisc.edu

- ¹⁴*Department of Physics, University of Maryland, College Park, MD, USA and NASA GSFC, Greenbelt, MD 20771, USA*
- ¹⁵*Department of Physics and Astronomy, University of California, Los Angeles, CA 90095, USA*
- ¹⁶*Department of Physics and Astronomy, University of Iowa, Van Allen Hall, Iowa City, IA 52242, USA*
- ¹⁷*Department of Physics and Astronomy, DePaul University, Greencastle, IN 46135-0037, USA*
- ¹⁸*DESY, Platanenallee 6, 15738 Zeuthen, Germany*
- ¹⁹*Department of Physics, University of Maryland, College Park, MD, USA*
- ²⁰*School of Natural Sciences, University of Galway, University Road, Galway, H91 TK33, Ireland*
- ²¹*School of Physics, University College Dublin, Belfield, Dublin 4, Ireland*
- ²²*Department of Physics and Astronomy, Ball State University, Muncie, IN 47306, USA and Department of Physics, Anderson University, 1100 East 5th Street, Anderson, IN 46012*
- ²³*Department of Physics and Astronomy, Barnard College, Columbia University, NY 10027, USA*
- ²⁴*Department of Physics, Engineering Physics and Astronomy, Queen University, Kingston, ON K7L 3N6, Canada*
- ²⁵*Institute of Physics and Astronomy, University of Potsdam, 14476 Potsdam-Golm, Germany and DESY, Platanenallee 6, 15738 Zeuthen, Germany*
- ²⁶*Fakultät für Physik & Astronomie, Ruhr-Universität Bochum, D-44780 Bochum, Germany*
- ²⁷*Department of Physics and Astronomy, Purdue University, West Lafayette, IN 47907, USA*
- ²⁸*Department of Physics, Indiana University-Purdue University Indianapolis, Indianapolis, IN 46202, USA*
- ²⁹*Department of Physics, University of Maryland, Baltimore County, Baltimore MD 21250, USA and NASA GSFC, Greenbelt, MD 20771, USA*
- ³⁰*Department of Physics and Astronomy, Iowa State University, Ames, IA 50011, USA*
- ³¹*Columbia Astrophysics Laboratory, Columbia University, New York, NY 10027, USA*
- ³²*Instituto de Física, Universidad Nacional Autónoma de México, Ciudad de México, Mexico*
- ³³*Universidad Autónoma de Chiapas, Tuxtla Gutiérrez, Chiapas, México*
- ³⁴*Universidad Michoacana de San Nicolás de Hidalgo, Morelia, Mexico*
- ³⁵*Department of Physics, Michigan Technological University, Houghton, MI, USA*
- ³⁶*Instituto de Astronomía, Universidad Nacional Autónoma de México, Ciudad de México, Mexico*
- ³⁷*Instituto Nacional de Astrofísica, Óptica y Electrónica, Puebla, Mexico*
- ³⁸*Instytut Fizyki Jadrowej im Henryka Niewodniczanskiego Polskiej Akademii Nauk, IFJ-PAN, Krakow, Poland*
- ³⁹*Facultad de Ciencias Físico Matemáticas, Benemérita Universidad Autónoma de Puebla, Puebla, Mexico*
- ⁴⁰*Department of Physics, University of Wisconsin-Madison, Madison, WI, USA*
- ⁴¹*Departamento de Física, Centro Universitario de Ciencias Exactas e Ingenierías, Universidad de Guadalajara, Guadalajara, Mexico*
- ⁴²*Max-Planck Institute for Nuclear Physics, 69117 Heidelberg, Germany*
- ⁴³*Department of Physics, Stanford University: Stanford, CA 94305-4060, USA*
- ⁴⁴*Tecnológico de Monterrey, Escuela de Ingeniería y Ciencias, Ave. Eugenio Garza Sada 2501, Monterrey, N.L., Mexico, 64849*
- ⁴⁵*Universidad Politécnica de Pachuca, Pachuca, Hgo, Mexico*
- ⁴⁶*Department of Physics and Astronomy, University of Utah, Salt Lake City, UT, USA*
- ⁴⁷*University of Seoul, Seoul, Rep. of Korea*
- ⁴⁸*Physics Division, Los Alamos National Laboratory, Los Alamos, NM, USA*
- ⁴⁹*Centro de Investigaci'ón en Computaci'ón, Instituto Politécnico Nacional, México City, México.*
- ⁵⁰*Dept of Physics and Astronomy, University of New Mexico, Albuquerque, NM, USA*
- ⁵¹*Universidad Autónoma del Estado de Hidalgo, Pachuca, Mexico*
- ⁵²*Department of Physics, Temple University, Philadelphia, PA, USA*
- ⁵³*Instituto de Ciencias Nucleares, Universidad Nacional Autónoma de México, Ciudad de México, Mexico*
- ⁵⁴*Department of Physics and Astronomy, Michigan State University, East Lansing, MI, USA*
- ⁵⁵*Tsung-Dao Lee Institute, Shanghai Jiao Tong University, Shanghai, China*
- ⁵⁶*NASA Goddard Space Flight Center, Greenbelt, MD 20781, USA*
- ⁵⁷*Department of Physics and Astronomy, University of Maryland, College Park, MD 20742, USA*

ABSTRACT

This paper investigates the origin of the γ -ray emission from MGRO J1908+06 in the GeV-TeV energy band. By analyzing the data collected by *Fermi*-LAT, VERITAS, and HAWC, with the addition of spectral data previously reported by LHAASO (Cao et al. 2021, 2023), a multiwavelength (MW) study of the morphological and spectral features of MGRO J1908+06 provides insight into the origin of the γ -ray emission. The mechanism behind the bright TeV emission is studied by constraining the magnetic field strength, the source age and the distance through detailed broadband modeling. Both spectral shape and energy-dependent morphology support the scenario that inverse-Compton (IC)

emission of an evolved pulsar wind nebula (PWN) associated with PSR J1907+0602 is responsible for the MGRO J1908+06 γ -ray emission with a best-fit true age of $T = 22 \pm 9$ kyr and a magnetic field of $B = 5.4 \pm 0.8 \mu\text{G}$, assuming the distance to the pulsar $d_{\text{PSR}} = 3.2$ kpc.

Keywords: MGRO J1908+06 — PSR J1907+0602 — pulsar wind nebulae — γ -ray astronomy

1. INTRODUCTION

In recent years, the HAWC and the LHAASO collaborations have reported the detection of energetic Galactic sources that are capable of emitting photons with energies above dozens of TeV, and many of these are spatially associated with pulsar wind nebulae (Abeysekara et al. 2020; Cao et al. 2021, 2023). The TeV detections of several PWNe by HAWC and LHAASO confirm that these objects are effective in accelerating particles up to the PeV regime. The acceleration mechanism and particle transport within PWNe can be understood through spectral and morphological studies. The age of the pulsar, the magnetic field inside the PWN, and the material surrounding the system such as the host supernova remnant (SNR) shell, are all key parameters for understanding the underlying physical processes and particle acceleration. The nearby middle-aged (10-100 kyr) PWNe are particularly interesting because these objects are close enough that GeV-TeV instruments can resolve complex morphologies, thus revealing the interaction of the PWN with the host SNR, which is expected to take place for the middle-aged systems, and particle radiative and transport processes.

MGRO J1908+06 was first discovered by the Milagro experiment (Abdo et al. 2007) at a median energy of ~ 20 TeV. The source features bright high-energy emission of about 1.36 C.U. (Crab Nebula unit) at 100 TeV (Cao et al. 2021) with extension reported by multiple TeV instruments including H.E.S.S. (0.34° in radius, Aharonian et al. 2009), VERITAS (0.44° in radius, Aliu et al. 2014), ARGO-YBJ6 (0.49° in radius, Bartoli et al. 2012), HAWC (0.52° in radius, Abeysekara et al. 2020), and LHAASO (0.43° in radius, Cao et al. 2021). A recent report by Kostunin et al. (2021) further showed that the source displays an energy-dependent morphology. While the origin of the MGRO J1908+06 emission remains unknown, the supernova remnant SNR G40.5-0.5 and pulsar (PSR J1907+0602) have been suggested by recent literature as the potential counterparts to the TeV emission (see e.g., Aliu et al. 2014). SNR G40.5-0.5, located at R.A., Dec. = $286.786^\circ, 6.498^\circ$ (J2000), has an estimated age of 20-40 kyr and an estimated distance of 5.5-8.5 kpc based on the relation of the surface brightness and the diameter of the SNR (Downes et al. 1980). A recent discovery of a radio pulsar PSR

J1907+0631 located near the center of the SNR suggests a distance of 7.9 kpc based on the dispersion measure of the pulsar (Lyne et al. 2017). Different distance estimations have also been suggested by associating molecular clouds with the remnant, including a distance of 3.4 kpc by Yang et al. (2006) and a distance of 8.7 kpc by Duvidovich et al. (2020). The nearby pulsar PSR J1907+0602, located at R.A., Dec. = $286.978^\circ, 6.038^\circ$ (J2000), was originally detected by the *Fermi* Large Area Telescope (*Fermi*-LAT) and has a spin-down power of $\dot{E} = 2.8 \times 10^{36}$ erg/s, a characteristic age of $t_c = 19.5$ kyr, and an estimated distance of 3.2 ± 0.6 kpc (Abdo et al. 2010). The pulsar, PSR J1907+0602, has been observed by the Chandra X-ray Observatory (Abdo et al. 2010) and the XMM-Newton X-ray satellite (Pandel & Scott 2012; Li et al. 2021). Pandel & Scott (2012) analyzed a 52-ks XMM-Newton observation and found a marginal excess separated from the pulsar by a distance of $7''$, which could be interpreted as a bow shock in front of the pulsar as it moved to its current location from the centroid of MGRO J1908+06. Abdo et al. (2010) reported some evidence for the spatial extent of the X-ray emission based on a 19-ks Chandra observation, which suggested a compact pulsar wind nebula. However, using a deeper exposure of 109-ks of XMM-Newton data, Li et al. (2021) found no extended nebula emission and that the X-ray emission is consistent with a point-like pulsar. The locations of PSR J1907+0602 and of SNR G40.5-0.5 can be found in Figure 1 overlaid with the TeV emission morphology.

On the origin of MGRO J1908+06 emission, a recent study of radio data by Duvidovich et al. (2020) found molecular clouds around the border of SNR G40.5-0.5 and suggested that the TeV emission is a combination of a leptonic component emitted by the PWN of PSR J1907+0602 and a hadronic component produced by the interaction between the molecular clouds and SNR G40.5-0.5. The two-component hypothesis is further explored in a multiwavelength analysis by Crestan et al. (2021), in which the authors concluded that the analysis result favors the two-component scenario with the GeV emission (10-1000 GeV) being leptonic, and the TeV emission having a hadronic origin. The two-component scenario is also supported by a spectral analysis including HAWC and LHAASO data (De Sarkar & Gupta

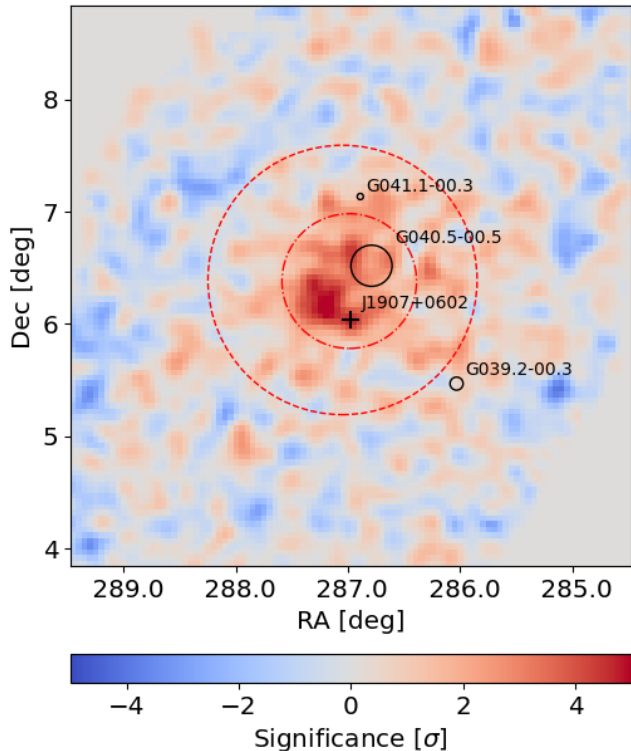


Figure 1. VERITAS γ -ray significance map in the energy range [0.5, 7.9] TeV. The black cross indicates the location of PSR J1907+0602, and the black circles outline the shell sizes of the SNRs in the region, including (middle) G40.5-0.5, (top) G041.1-00.3, and (bottom) G039.2-00.3. The red dashed circle shows the region of interest in which the VERITAS spectrum is extracted from, and the red dash-dot circle shows the best-fit Gaussian radius in the Fermi-LAT data. The color scale is limited to a range of $(-5, +5)$.

2022). In addition to the TeV emission, extended GeV emission at the vicinity of PSR J1907+0602 is found in an analysis of *Fermi*-LAT data by Li et al. (2021), where a low-energy (< 10 GeV) component is said to be hadronic emission originating from the interaction between the SNR and nearby molecular clouds, while the high-energy (> 10 GeV) component is likely to be the inverse Compton emission of the PWN associated to PSR J1907+0602.

While it has been indicated by previous works that both the PWN and the nearby SNR are plausible contributors to both the GeV and TeV emission, it remains unknown to what degree. This paper reports a new energy-dependent morphological study of MGRO J1908+06 using the *Fermi*-LAT, VERITAS, and HAWC observations and multiwavelength spectral modeling across the GeV-TeV energy domain to provide new insights into the origin of the MGRO J1908+06 emission, taking into consideration as well the absence of an X-

ray detection of the nebula. Section 2, 3, 4 describe the *Fermi*-LAT, VERITAS, and HAWC data analyses and results, respectively. Section 5 explores possible scenarios for the MGRO J1908+06 emission, including a leptonic explanation in Section 5.1 and a hadronic explanation in Section 5.2. The preferred scenarios for the MGRO J1908+06 are summarized in Section 6.

2. FERMI-LAT DATA ANALYSIS

The principal scientific instrument on the Fermi Gamma-ray Space Telescope is the Large Area Telescope (LAT, Atwood et al. 2009). The LAT instrument is sensitive to γ -rays with energies from 50 MeV to > 300 GeV (Abdollahi et al. 2020). The instantaneous field of view of LAT is ~ 2.4 steradian and has been continuously surveying the entire sky every 3 hours since beginning operation in 2008 August. The on-axis effective area at 1 GeV is close to 8000 cm^2 , rises to 9000 cm^2 at 2 GeV and remains constant until 500 GeV. The point spread function (PSF, 68% containment radius) at 1 GeV is $< 1^\circ$ and becomes $\sim 0.1^\circ$ above 10 GeV.

We analyze just over 14 years (from 2008 August to 2022 November) of Pass 8 SOURCE class data (Atwood et al. 2013; Bruel et al. 2018) between 30 GeV and 2 TeV, similar to Li et al. (2021), but with 3 more years of *Fermi*-LAT data. The energy range for the analysis is motivated by avoiding contamination from the γ -ray pulsar J1907+0602 below 30 GeV in addition to the possible hadronic component $E < 10$ GeV as presented in Li et al. (2021). Photons detected at zenith angles larger than 90° were excluded to limit the contamination from γ -rays generated by cosmic ray (CR) interactions in the upper layers of the Earth’s atmosphere. We do not require pulsar gating of the GeV PSR J1907+0602, since the magnetospheric emission from PSR J1907+0602 exhibits a spectral cutoff at 2.9 GeV and is not significant at energies above 30 GeV (Abdo et al. 2013; Li et al. 2021). Aside from the *Fermi*-LAT detection of the pulsar, there is no Fermi counterpart in the 4FGL catalog associated with MGRO J1908+06 (Abdollahi et al. 2022).

We perform a joint likelihood analysis of events according to their PSF type (PSF0, PSF1, PSF2, and PSF3) using the latest Fermitools package¹ (v.2.2.11) and FermiPy Python 3 package (v.1.2.0 Wood et al. 2017). Details of the analysis are provided in Appendix A.

Figure 2 (a) displays the 30 – 300 GeV residual excess counts map centered on MGRO J1908+06. The residual

¹ <https://fermi.gsfc.nasa.gov/ssc/data/analysis/software/>

excess counts map shows significant unmodeled residuals coincident to the MGRO J1908+06 source. The excess corresponds to a 3σ significance test statistic (TS, see Appendix A).

2.1. *Fermi*-LAT Data Analysis Results

To model the γ -ray emission excess coincident with MGRO J1908+06, we first add a point source at the TeV PWN location R.A., Dec. = 287.11° , $+6.21^\circ$ (J2000) to the 30 GeV–2 TeV source model. We set the spectrum to a power law,

$$\frac{dN}{dE} = N_0 \left(\frac{E}{E_0} \right)^{-\Gamma_\gamma}, \quad (1)$$

where E_0 is set to 1000 MeV. We allow the spectral index and normalization to vary. We localize the point source with `GTAnalysis.localize` to find the best-fit position and uncertainty. The localized position for the new γ -ray source is offset by 0.4° from the exact position of PSR J1907+0602, corresponding to the nearby peak excess (Fig 2 (a)) and has R.A., Dec. = 287.25° , $+6.21^\circ$ (J2000). The corresponding 95% positional uncertainty radius is $r_{95} = 0.10^\circ$. The TS of the γ -ray source is 16 at this location with a spectral index $\Gamma_\gamma = 2.50 \pm 0.40$, corresponding to a significance at the 3σ level.

We run extension tests on the best-fit point source utilizing `GTAnalysis.extension` and the two spatial templates supported in the FermiPy framework, the radial disk and radial Gaussian templates. Both of these extended templates assume a symmetric 2D shape with width parameters radius and sigma, respectively. We allow the position and spectral parameters to vary when finding the best-fit spatial extension in both cases. The best-fit parameters for the extension tests are presented in Table 1. The radial Gaussian template is chosen to describe the γ -ray morphology and is found to have $\text{TS}_{\text{ext}} = 34.9$ ($\text{TS}_{\text{ext}} = 2 \times \ln\left(\frac{L_{\text{ext}}}{L_{\text{ps}}}\right)$) and an extension $\sigma = 0.60^\circ \pm 0.10^\circ$ at the location R.A., Dec. = 286.99° , $+6.38^\circ$ (J2000) with a 95% uncertainty for the centroid position that is $r_{95} = 0.30^\circ$. The TS and best-fit power-law index for the radial Gaussian source is 37.4 and $\Gamma_\gamma = 1.80 \pm 0.10$, respectively.

The results reported here are in reasonable agreement with the prior *Fermi*-LAT analysis from Li et al. (2021), where they found that a radial disk template with $r = 0.51 \pm 0.02^\circ$ located at R.A., Dec. = 286.88° , $+6.29^\circ$ (J2000) best characterized the extended γ -ray emission along with a power-law spectrum best-fit with $\Gamma_\gamma = 1.60 \pm 0.20$. The integrated energy flux for the 30 GeV–2 TeV energy band is $3.40 \pm 0.90 \times 10^{-11}$ erg $\text{cm}^{-2} \text{s}^{-1}$, consistent with Li et al. (2021).

3. VERITAS DATA ANALYSIS

VERITAS (the Very Energetic Radiation Imaging Telescope Array System) is an array of four imaging atmospheric Cherenkov telescopes (IACTs) located at the Fred Lawrence Whipple Observatory in Arizona, USA (Weekes et al. 2002). Each telescope consists of a 12-m diameter reflector and a camera of 499 photomultiplier tube (PMT) pixels, covering a field of view of 3.5° . VERITAS is sensitive to photons in the energy range from 100 GeV to 50 TeV with an optimal angular resolution of 0.08° (68% containment radius) above 1 TeV. The VERITAS data used in this study are collected during the period between 2009 and 2022. After data quality selection, an effective total of 128 hours of exposure is available around the location of MGRO J1908+06.

3.1. VERITAS Background Estimation Methods

MGRO J1908+06 is an extended source in the TeV band. The associated source 3HWC J1908+063 is reported with a best-fit diffusion radius $\theta_d = 1.78 \pm 0.08_{-0.02}^{+0.07}$ degrees (Albert et al. 2022). This is comparable to the 3.5° diameter of the VERITAS field of view, requiring an alternative to the background-estimation methods that are typically used which estimate the background from the observations by using signal-free regions of the FoV. Thus, a novel background estimation method (Low-rank Perturbation method, LPM) is developed and described in Section B.1. The LPM utilizes the distributions of cosmic-ray-like events collected from the MGRO J1908+06 observations that failed the γ -ray event selection and events from archival γ -ray-free observations to derive a background estimation for γ -ray-like background events. The LPM does not rely on the source morphology assumption and is able to analyze a source with an angular size larger than the field of view of the instrument. An independent background method is used as a cross check for the LPM analysis. The results of the cross-check analyses can be found in Section B.3.

It is noted that the diffuse γ -ray emission from the Galactic plane is not included in the background model for the VERITAS analysis, since the Galactic plane emission is not significantly detected in the VERITAS γ -ray significance map (see Figure 1) as well as the γ -ray brightness radial profile (see Figure 10).

3.2. VERITAS Data Analysis Results

The VERITAS data and the LPM background method allow the measurement of the entirety of MGRO J1908+06 emission covering a large region with a radius up to 2.5° centered at the 3HWC J1908+063 centroid. The radial profile of the MGRO J1908+06 emission is shown in Figure 10. An integrated VERITAS

Spatial Template	TS	TS _{ext}	(R.A., Dec.) (°, J2000)	r or σ (°)	95% U.L. (°)
Point Source	15.8	–	287.25, +6.21	–	–
Radial Disk	38.4	21.9	286.87, +6.30	0.44 ± 0.03	0.48
Radial Gaussian	37.4	34.9	286.99, +6.38	0.60 ± 0.10	0.81

Table 1. Summary of the best-fit parameters and the associated statistics for each spatial template used in our *Fermi*-LAT analysis. The final column represents the 95% upper limit for the extension.

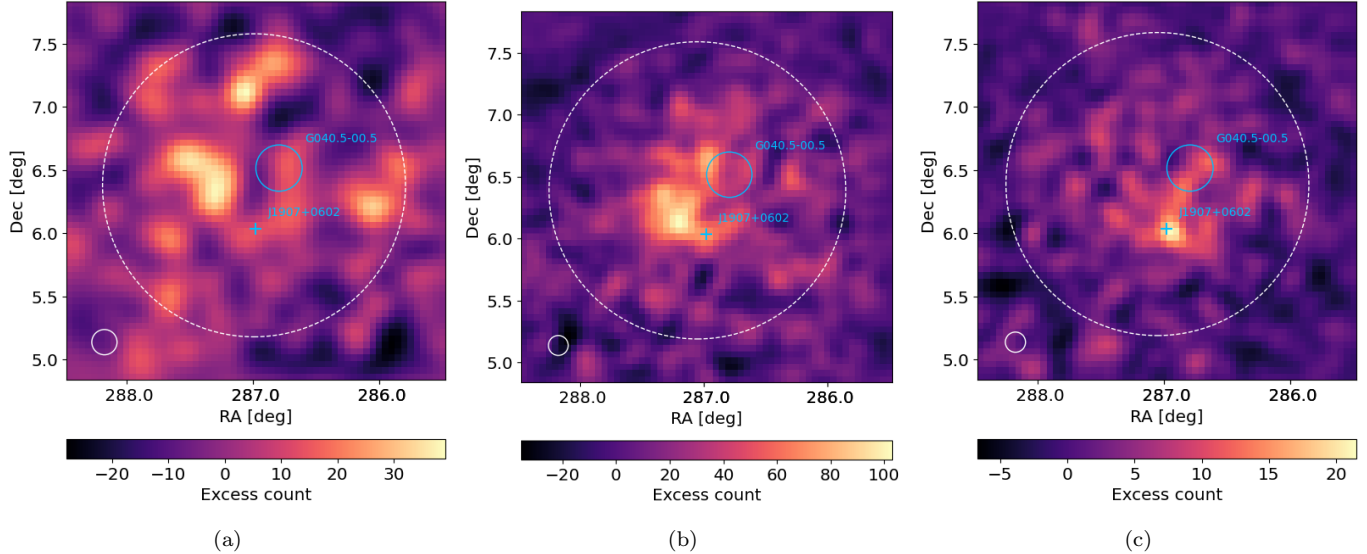


Figure 2. (a) *Fermi*-LAT γ -ray residual map in the energy range [30, 300] GeV overlaid with a white dashed circle showing the 95.5% containment of the γ -ray photons. (b) VERITAS γ -ray residual map in the energy range [0.5, 2.0] TeV overlaid with a white dashed circle showing the extraction region of the γ -ray spectrum. (c) VERITAS γ -ray residual map in the energy range [2.0, 7.9] TeV overlaid with a white dashed circle showing the extraction region of the γ -ray spectrum. The sky-blue cross indicates the location of PSR J1907+0602, and the sky-blue circle outlines the shell size of SNR G40.5-0.5. The white solid circles indicate the size of PSF of the corresponding instrument. The coordinates are in J2000 equatorial degrees.

significance map is shown in Figure 1 in the energy range [0.5, 7.9] TeV. Figure 2 (b) and Figure 2 (c) show the energy-dependent γ -ray residual excess map of MGRO J1908+06 in the VERITAS data for [0.5, 2.0], and [2.0, 7.9] TeV bins, respectively. In the [0.5, 2.0] TeV bin, the core emission is near but not centered around the location of PSR J1907+0602. The core emission then becomes more concentrated around the pulsar at the higher energies in [2.0, 7.9] TeV. The energy-dependent morphology of MGRO J1908+06 has also been reported by Kostunin et al. (2021) and showed a similar trend. After correcting for the effect of off-axis γ -ray acceptance, a Gaussian model is fit to the γ -ray morphology in the energy ranges of [0.5, 2.0] TeV and [2.0, 7.9] TeV. The energy-dependent Gaussian centroid locations and radii are shown in Table 4.

An analysis region centered at the 3HWC J1908+063 centroid R.A., Dec. = 287.05°, 6.39° (Albert et al. 2022) with a radius of 1.2° is used to study the spectrum of MGRO J1908+06. It is assumed that the γ -

ray morphology reflects the underlying particle distribution, thus, the VERITAS analysis region is designed to cover an area that contains the majority of emissions in *Fermi*-LAT and HAWC data. The VERITAS analysis region is highlighted by the white dashed circle in Figure 2 (b) and (c). The VERITAS flux is calculated from the events included within the region. The breakdown infor-

Energy [TeV]	Count	Background	$E^2 \frac{dN}{dE}$ [TeV cm ⁻² s ⁻¹]	σ
0.50-0.75	36435	$34696 \pm 190 \pm 303$	$(9.2 \pm 1.1 \pm 2.0) \times 10^{-12}$	4.9
0.75-1.26	19851	$18068 \pm 140 \pm 170$	$(10.1 \pm 0.8 \pm 1.0) \times 10^{-12}$	8.1
1.26-2.00	9448	$7814 \pm 97 \pm 187$	$(12.1 \pm 0.7 \pm 1.3) \times 10^{-12}$	7.7
2.00-3.16	3803	$3049 \pm 61 \pm 79$	$(7.9 \pm 0.6 \pm 0.8) \times 10^{-12}$	7.5
3.16-5.01	1357	$984 \pm 36 \pm 55$	$(5.9 \pm 0.7 \pm 0.9) \times 10^{-12}$	5.6
5.01-7.94	547	$290 \pm 23 \pm 20$	$(6.6 \pm 1.1 \pm 0.5) \times 10^{-12}$	8.2

Table 2. The energy-dependent VERITAS data count, background (with statistical and systematic uncertainties), flux (with statistical and systematic uncertainties), and detection significance σ in the region of interest with a radius of 1.2° centered at the 3HWC J1908+063 centroid.

mation in the region of analysis, including data count, background and uncertainties, are summarized in Table 2. The VERITAS spectrum of MGRO J1908+06 is shown in Figure 3 along with the spectra of *Fermi*-LAT (Section 2), HAWC (Section 4), and LHAASO data (Cao et al. 2021, 2023).

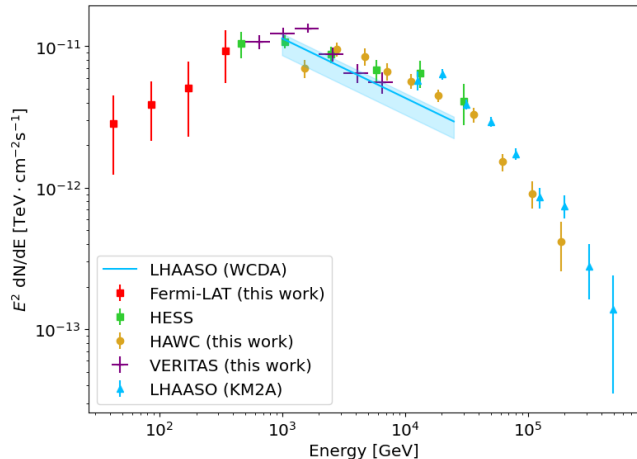


Figure 3. The multiwavelength spectrum of MGRO J1908+06. The red points represent the data in this work for *Fermi*-LAT data in [30, 300] GeV, the purple points represent VERITAS data in [0.5, 7.9] TeV, the lime green points represent H.E.S.S. data (Kostunin et al. 2021), the golden points represent HAWC data in [1.1, 246] TeV, and the sky blue points represent LHAASO data in [10, 625] TeV (Cao et al. 2021, 2023). The *Fermi*-LAT data are truncated at 300 GeV because of the low statistics at the higher energies.

4. HAWC DATA ANALYSIS

The High Altitude Water Cherenkov (HAWC) gamma-ray observatory located in Puebla, Mexico surveys the sky in the 300 GeV to > 100 TeV energy range and has been able to detect the source 3HWC J1908+063 which is 0.29° apart from MGRO J1908+06 and that has been reported in Albert et al. (2022). For this work, we use the HAWC Data Pass 5 Albert et al. (2024) that comprises 2321 days of observations collected between November 2014 and October 2021. The data set is divided in bins according to the fraction of photo-multiplier tubes that are triggered in each shower event which are then sub-divided into 12 quarter-decade energy bins covering the 0.316-316 TeV range. This is performed using the ground parameter method presented in Abeyssekara et al. (2019a), which uses the fit to the lateral distribution function to measure the charge density 40 meters from the shower core, along with the zenith angle of the air shower, to estimate the energy of the primary gamma ray.

To perform the spectral and spatial fit, a maximum likelihood technique is used with the Multi-Mission Maximum Likelihood (3ML) framework (Vianello et al. 2015) with the HAWC Accelerated Likelihood (HAL) plug-in (Abeyssekara et al. 2021). To determine the significance of the fit, we use the likelihood ratio test statistic (TS) which is defined by

$$TS = 2 \ln \left(\frac{\mathcal{L}_{S+B}}{\mathcal{L}_B} \right), \quad (2)$$

where \mathcal{L}_{S+B} is the maximum likelihood of a signal plus background model, which depends on the spectral and spatial parameters, and \mathcal{L}_B is the maximum likelihood of the background-only hypothesis.

The region of interest to model the emission is centered at J2000 R.A. = 287.70° and Dec. = 5.45° with a radius of 3 degrees which includes 3 sources: 3HWC J1908+063 and the east and west lobes of a nearby microquasar, SS433 (Abeyssekara et al. 2018). Additionally we included the Galactic diffuse emission (GDE) contribution. A Gaussian model is chosen to describe MGRO J1908+06, rather than the diffusion-based source model used by Albert et al. (2022). The reason for choosing the Gaussian model over the diffusion-based source model is that the characteristic age of the PSR J1907+0602 (19.5 kyr) indicates that the system is evolved but not old enough for the diffusion process to be the dominant mode of particle transport. The spectrum of MGRO J1908+06 is modeled as a log-parabola:

$$\frac{dN}{dE} = K \left(\frac{E}{10 \text{ TeV}} \right)^{-\alpha - \beta \ln(E/10 \text{ TeV})}, \quad (3)$$

where K is the normalization flux, α is the spectral index and β is the curvature; these three parameters are left free in the fit.

The SS433 lobes are modeled as point-like sources with fixed position (Abeyssekara et al. 2018) and with power-law spectra:

$$\frac{dN}{dE} = K \left(\frac{E}{10 \text{ TeV}} \right)^{-2.0}, \quad (4)$$

The GDE is modeled with a Gaussian distribution centered in the Galactic plane, and described by power-law spectrum with index -2.75 (Abdo et al. 2008; Zhou et al. 2017); both the Gaussian width σ and the normalization flux are left free in the fit.

4.1. HAWC Data Analysis Results

The HAWC γ -ray significance maps in the energy range [3.16, 100] TeV are shown in Figure 4. These HAWC maps show a consistent trend of correlation between the TeV emission and the pulsar PSR

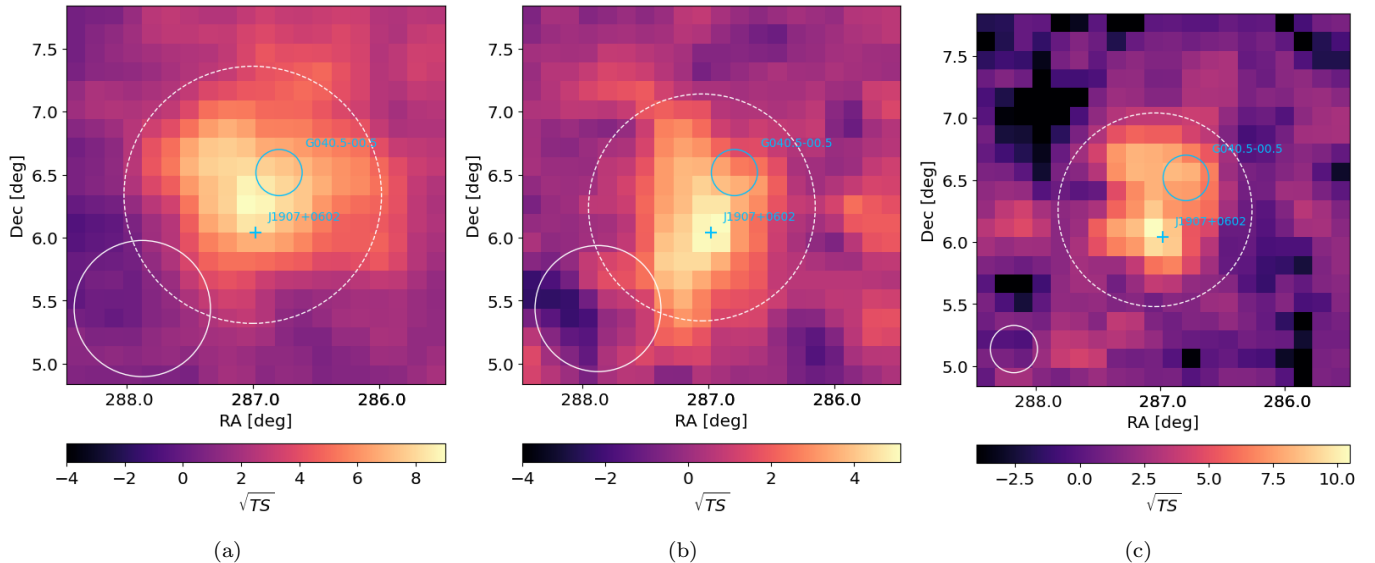


Figure 4. HAWC γ -ray significance map in the energy range (a) [3.16, 10] TeV, (b) [10, 31.6] TeV, and (c) [31.6, 100] TeV, overlaid with the white a dashed circle showing the 95.5% containment of the γ -ray photons in each energy range. The sky-blue cross indicates the location of PSR J1907+0602, and the sky-blue circle outlines the shell sizes of the SNR G40.5-0.5. The white solid circles indicate the size of PSF of the HAWC instrument in the corresponding energy range. The coordinates are in J2000 equatorial degrees.

J1907+0602, where the γ -ray emission is seen to be more concentrated around the pulsar at higher energies. For MGRO J1908+06, the best-fit normalization flux is $K = (4.82 \pm 0.19) \times 10^{-14} \text{ TeV}^{-1} \text{ cm}^{-2} \text{ s}^{-1}$, spectral index $\alpha = 2.320 \pm 0.022$, curvature $\beta = 0.140 \pm 0.015$ and extension $\sigma = 0.^\circ 475 \pm 0.^\circ 013$. The list of best-fit parameters, including those of the other three sources and systematic uncertainties, is shown in Table 3. The resulting TS values for MGRO J1908+06, SS433E, SS433W and the GDE are 2050.05, 44.0, 63.7 and 276.9, respectively. In order to obtain the energy-dependent morphology of the source, the Gaussian model is fitted to the HAWC data in five energy bins: [1.0, 3.16, 10.0, 31.6, 100, 316] TeV, and the centroid and the extension of the source in three of the energy bins are reported in Table 4.

Compared to the previous results reported in Albert et al. (2022), a larger TS is reported in this work, with $\Delta TS = 120$. The flux normalization also varies by $\sim 50\%$ compared to the previously reported value. The difference between the flux normalization presented by this work and the one presented by Albert et al. (2022) is largely due to the choice of the morphological model. In Albert et al. (2022), the nominal spatial model is the diffusion-based source model, which has a long tail and gives a flux normalization that is $\sim 2\times$ higher than the normalization given by a Gaussian model with the extent fixed to the IACT extent of 0.44° at γ -ray energy in [1, 10] TeV. The higher HAWC flux normalization provided by the diffusion model might be overestimated due

to the poor angular resolution in the energy range between 1 and 10 TeV (HAWC γ -ray PSF is 0.64° at 1 TeV and 0.50° at 10 TeV) that could lead to an overestimated morphology tail and an overestimated flux. The HAWC PSF improves at higher energies (0.19° at 30 TeV), and the fluxes reported by the diffusion-based source model and the Gaussian model in Albert et al. (2022) become more consistent at γ -ray energy beyond 30 TeV. Additionally, this work utilizes the HAWC Data Pass 5 Albert et al. (2024), which incorporates an updated reconstruction algorithm that offers better sensitivity at lower energies compared to the Data Pass 4 used in Albert et al. (2022).

5. EMISSION MODELS FOR MGRO J1908+06

5.1. Leptonic PWN model

In this section, the TeV emission in [0.03, 625] TeV is assumed to be the IC emission from a PWN. The multiwavelength spectral energy distribution (SED) data in Figure 3 are fitted using the NAIMA python package (Zabalza 2015). The electron spectral model is

$$f(d_{\text{PSR}}, E) = \begin{cases} A(d_{\text{PSR}}) \left(\frac{E}{E_0}\right)^{-\alpha}, & \text{if } E < E_{\text{break}} \\ A(d_{\text{PSR}}) \left(\frac{E_{\text{break}}}{E_0}\right)^\beta \left(\frac{E}{E_0}\right)^{-\alpha-\beta}, & \text{if } E > E_{\text{break}} \end{cases} \quad (5)$$

where E is the electron energy, d_{PSR} is the distance between the pulsar and the observer, $E_0 = 1 \text{ TeV}$ is

Parameter	Best-fit value
MGRO J1908+06	
σ	$0.^\circ 475 \pm (0.^\circ 013)_{\text{stat}} \left(\begin{smallmatrix} +0.009 \\ -0.014 \end{smallmatrix} \right)_{\text{sys}}$
K	$[4.82 \pm (0.19)_{\text{stat}} \left(\begin{smallmatrix} +0.44 \\ -1.4 \end{smallmatrix} \right)_{\text{sys}}] \times 10^{-14}$
α	$2.320 \pm (0.022)_{\text{stat}} \left(\begin{smallmatrix} +0.045 \\ -0.063 \end{smallmatrix} \right)_{\text{sys}}$
β	$0.140 \pm (0.015)_{\text{stat}} \left(\begin{smallmatrix} +0.083 \\ -0.027 \end{smallmatrix} \right)_{\text{sys}}$
SS 433 east and west lobes	
K_{SS433E}	$[1.00 \pm (0.28)_{\text{stat}} \left(\begin{smallmatrix} +0.18 \\ -0.16 \end{smallmatrix} \right)_{\text{sys}}] \times 10^{-16}$
K_{SS433W}	$[3.45 \pm (0.59)_{\text{stat}} \left(\begin{smallmatrix} +0.13 \\ -0.42 \end{smallmatrix} \right)_{\text{sys}}] \times 10^{-16}$
Galactic Diffuse Emission	
σ_{GDE}	$1.^\circ 40 \pm (0.^\circ 11)_{\text{stat}} \left(\begin{smallmatrix} +0.037 \\ -0.009 \end{smallmatrix} \right)_{\text{sys}}$
K_{GDE}	$[5.74 \pm (0.33)_{\text{stat}} \left(\begin{smallmatrix} +0.12 \\ -0.18 \end{smallmatrix} \right)_{\text{sys}}] \times 10^{-15}$

Table 3. HAWC best-fit results. The normalization flux values K , K_{SS433E} , K_{SS433W} and K_{GDE} have units of $\text{TeV}^{-1} \text{cm}^{-2} \text{s}^{-1}$.

the reference energy, $A(d_{\text{PSR}})$ is the distance-dependent number of electrons per unit energy, E_{break} is the synchrotron cooling break, $\alpha = 2$ is the electron injection index, and β is the spectral softening factor due to radiative cooling.

The far-infrared (FIR) field is expected to have noticeable impact to the IC spectrum in addition to the field of Cosmic Microwave Background (CMB) (Breuhaus et al. 2021). The data of the target photon field in the far-infrared band (0.27 THz - 8.82 THz) are obtained using the R12 and F98 ISRF models that were published in Porter et al. (2017). The energy density spectrum of the target photon field is approximated with a black-body radiation of a temperature of 51.6 K and an energy density of 0.074 eV/cm^3 .

The best-fit parameters are: $A(d_{\text{PSR}}) = (7.5 \pm 0.8) \times 10^{45} \times (d_{\text{PSR}}/\text{kpc})^2 \text{ TeV}^{-1}$, $E_{\text{break}} = 17.2 \pm 1.0 \text{ TeV}$, and $\beta = 1.37 \pm 0.02$. The result of the fit can be seen in Figure 6.

During the PWN evolution, constant expansion velocity and adiabatic-dominated energy losses are assumed. In this case, the energy change rate in the PWN is

$$\frac{dE_{\text{PWN}}}{dt} = \dot{E}(t) - \frac{E_{\text{PWN}}}{t}, \quad (6)$$

where E_{PWN}/t is the adiabatic energy loss due to the expansion, and $\dot{E}(t)$ is the time-dependent energy injection from the pulsar spin-down power,

$$\dot{E}(t) = \dot{E}_0 \left(1 + \frac{t}{\tau_0} \right)^{-(n+1)/(n-1)}, \quad (7)$$

where n is the braking index, τ_0 is the spin-down timescale, and $\dot{E}(t = T) = 2.8 \times 10^{36} \text{ erg/s}$ is the current spin-down power of PSR J1907+0602, $t = T$ is the

true age for PSR J1907+0602. Using the initial condition that PWN has zero energy at $t = 0$, the solution to Equation 6 is

$$\epsilon = \frac{(1+x)^{1-y}}{1-y} - \frac{(1+x)^{2-y}}{x(1-y)(2-y)} + \frac{1}{x(1-y)(2-y)}, \quad (8)$$

where $\epsilon = E_{\text{PWN}}/\dot{E}_0\tau_0$, $x = t/\tau_0$, and $y = (n+1)/(n-1)$ (Gelfand et al. 2009).

The electron SED parameter $A(d_{\text{PSR}})$ is connected to the PWN energy E_{PWN} through the energy fraction in leptons $\chi_e(d_{\text{PSR}}, T)$, i.e.

$$\int_{E_1}^{\infty} E f(d_{\text{PSR}}, E) dE = \chi_e(d_{\text{PSR}}, T) E_{\text{PWN}}(T), \quad (9)$$

where $E_1 = 0.1 \text{ GeV}$ is adopted, assuming it to be similar to the inferred value of the Crab Nebula (Büsching et al. 2008), and $f(d_{\text{PSR}}, E)$ is the electron spectrum defined in Equation 5.

By equating the true age T and the electron cooling time t_{cool} , the measured E_{break} in the *Fermi*-VERITAS-HAWC multiwavelength data connects the true age T and the energy density of the magnetic field,

$$T = t_{\text{cool}} \approx 300 \left(\frac{E_{\text{break}}}{\text{TeV}} \right)^{-1} \left(\frac{U_{\text{B}} + U_{\text{rad}}}{\text{eV cm}^{-3}} \right)^{-1} \text{ kyr}, \quad (10)$$

where U_{rad} is the combined energy density of CMB and FIR fields, and

$$U_{\text{B}}(T) = 6.24 \times 10^5 \times \frac{1}{8\pi} \times \left(\frac{B(T)}{\mu\text{G}} \right)^2 \text{ eV} \cdot \text{m}^{-3} \quad (11)$$

is the magnetic field energy density. The estimated $U_{\text{B}}(T)$ can be further used to estimate the energy fraction in magnetic field χ_{B} . Assuming a uniform magnetic field energy density in a volume

$$V_{\text{B}}(d_{\text{PSR}}) = \frac{4\pi}{3} \left(\frac{\pi}{180^\circ} \theta_{\text{d}} d_{\text{PSR}} \right)^3, \quad (12)$$

where $\theta_{\text{d}} \sim 0.48^\circ$ is the Gaussian radius at $E_\gamma = [0.5, 7.9] \text{ TeV}$, and d_{PSR} is the distance to the pulsar, one can derive the efficiency $\chi_{\text{B}}(d_{\text{PSR}}, T)$ via

$$U_{\text{B}}(T) V_{\text{B}}(d_{\text{PSR}}) = \chi_{\text{B}}(d_{\text{PSR}}, T) E_{\text{PWN}}(T). \quad (13)$$

Assuming that $\chi_e + \chi_{\text{B}} = 1$, one can constrain the pulsar true age and the distance to the pulsar using the observed γ -ray spectrum and morphology. Taking the spin-down timescale τ_0 to be in the range between an upper limit of 12 kyr (Aharonian et al. 1995; Abeysekara et al. 2017) and a lower limit of 0.72 kyr (Bucciantini et al. 2004), and $n = 2.4$ as the apparent braking index averaged from multiple radio pulsars (Young et al.

2010), Figure 5 shows the measured energy fraction sum $\chi_e + \chi_B$ as a function of the pulsar true age and distance to the pulsar. For models of young ages and large distances, the pulsar does not have sufficient energy to support the observed γ -ray flux and angular extension. On the contrary, the models of old ages and small distances could provide too much energy for the observed flux and extension. If one allows a range of the spin-down timescale $\tau_0 \in [0.72, 12]$ kyr, the two solid lines in Figure 5 indicate the parameter space of the most probable age and distance of the pulsar.

The distance to PSR J1907+0602 is estimated to be 3.2 ± 0.6 kpc using a dispersion measure (Abdo et al. 2010). Figure 5 places an estimate on the true age of the pulsar at $T = 22 \pm 9$ kyr and a total energy $W_e = 1.5 \times 10^{48}$ erg in electrons above 0.1 GeV. Assuming the pulsar true age $T = 22$ kyr and a distance $d_{\text{PSR}} = 3.2$ kpc, the IC spectral fitting yields $B = 5.4 \pm 0.8 \mu\text{G}$. Note that the estimated B field is in good agreement with the result presented by Li et al. (2021). The result of the fit using data from *Fermi*-LAT, VERITAS, HAWC, and LHAASO is shown as the solid blue curve in Figure 6.

It should be noted that the null detection of the PWN in X-ray band provides a strong constraint on the age and the distance of the pulsar. Li et al. (2021) used a region with a radius of 0.34° around the emission reported by Aharonian et al. (2009) and obtained an upper limit for MGRO J1908+06 of $1.2 \times 10^{-10} \text{erg s}^{-1} \text{cm}^{-2}$. The γ -ray morphology of MGRO J1908+06 has an Gaussian radius of 0.53° at 1 TeV, we thus scale up the XMM upper limit by a factor of $(0.53/0.34)^2 = 2.4$. The pulsar true age needs to be > 3.5 kyr, and the distance needs to be > 0.6 kpc, in order to keep the synchrotron emission below the scaled XMM upper limit (dashed curve in Figure 6).

5.2. Hadronic SNR model

To investigate the hadronic emission scenario of MGRO J1908+06, the HI and ^{12}CO (J=1-0) emission line data are studied to estimate the particle density in the region of the γ -ray source. The HI data are obtained through the GALFA HI Data Archive of the Arecibo L-band Feed Array (ALFA) at the NAIC Arecibo Observatory 305-meter radio telescope as is presented in Peek et al. (2017). The ^{12}CO (J=1-0) data are obtained through the whole-Galaxy CO survey presented in Dame et al. (2001) and the data files are downloaded from the 1.2 Meter CO Survey Dataverse of Smithsonian Astrophysical Observatory.

The velocity of the atomic and molecular emission is converted to a corresponding distance using the rotation curve model described in Bhattacharjee et al.

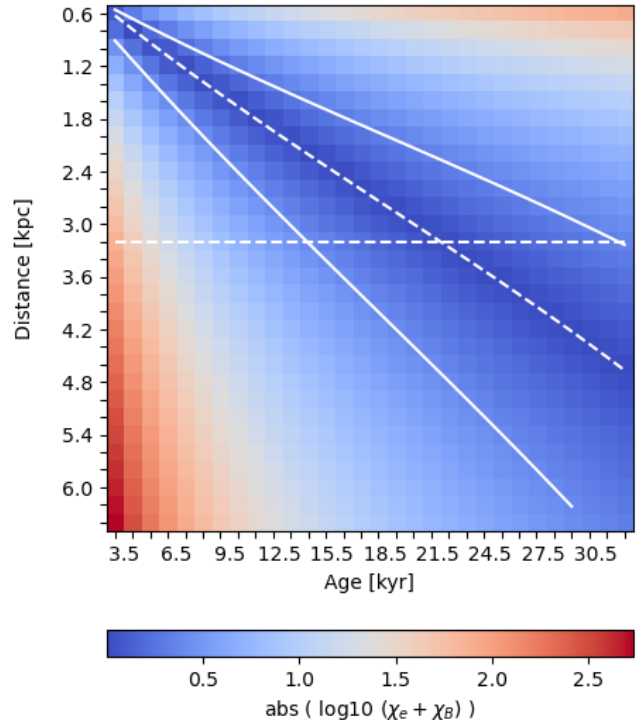


Figure 5. The measured energy fraction sum $\chi_e + \chi_B$ as a function of the pulsar true age and distance to the pulsar, and the distance estimation derived from a dispersion measure (Abdo et al. 2010) is shown as the white horizontal dashed line. The solid boundaries are derived from the upper and lower limits on the pulsar spin-down time scale, $\tau_0 \in [0.72, 12]$ kyr, and the diagonal dashed curve is derived from a medium value of $\tau_0 = 3$ kyr.

(2014) with the Galacto-centric distance $R_0 = 7.5$ kpc and the rotation velocity of the Sun $V_0 = 190$ km/s. The particle column density is calculated as $N_{\text{gas}} = X_{\text{gas}} \int T_{\text{gas}} dv [\text{cm}^{-2}]$, where T_{gas} is the brightness temperature of the atomic/molecular gas in K, v is the gas velocity in km/s, $X_{\text{HI}} = 1.82 \times 10^{18} \text{cm}^{-2} K \text{km s}^{-1}$ (Duvivovich et al. 2020), and $X_{\text{CO}} = 2 \times 10^{20} \text{cm}^{-2} K \text{km s}^{-1}$ (Bolatto et al. 2013). The integration of the gas emission is performed with velocity intervals of 2 km/s from $v = 2$ km/s to $v = 74$ km/s (corresponding to $z = 0.13$ kpc and $z = 5.71$ kpc), and the particle density is estimated in each velocity interval as $\rho = N/\Delta z$, where Δz is the corresponding distance interval. Three selected maps of atomic and molecular gas densities in the region of MGRO J1908+06 are shown in Figure 7. The gas density in the region containing the TeV emission is measured. The region is centered at the TeV emission centroid (RA,Dec) = $(287.05^\circ, 6.39^\circ)$ with a radius of 0.96° containing 95% of the TeV emission and is labeled by the red dashed circle in Figure 7. The measured gas densities in the region are shown in Figure 8. Both the

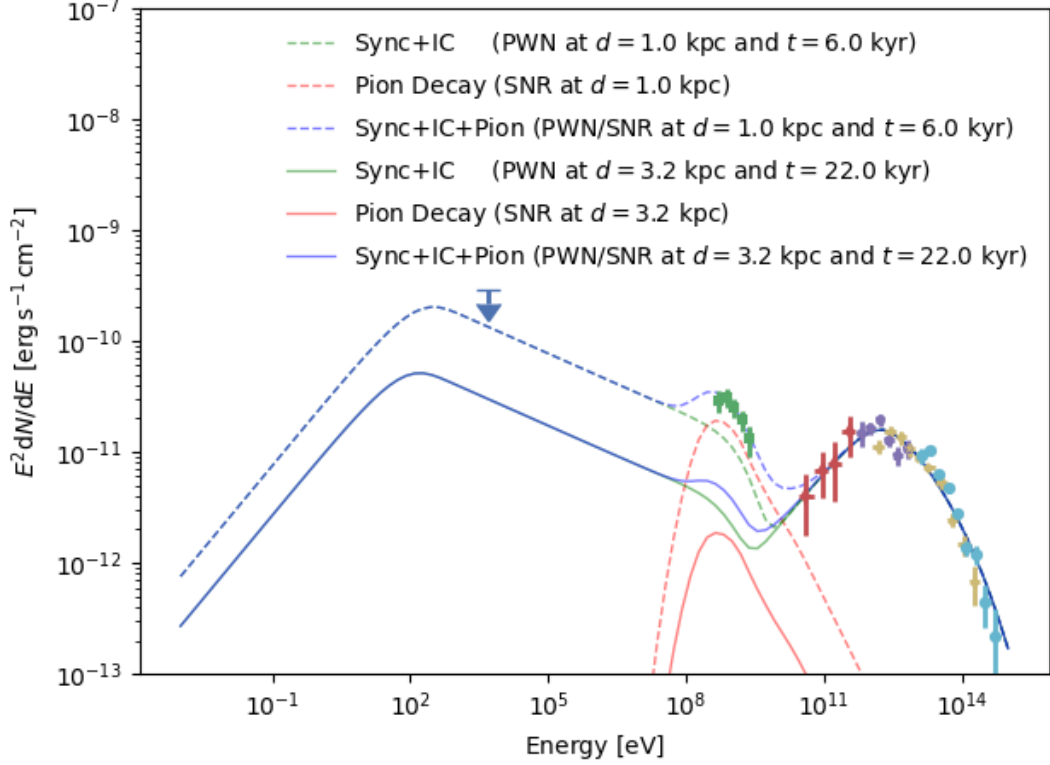


Figure 6. The MW SED data overlaid with the spectra of various emission models. The blue arrow represents the XMM-Newton upper limit (Li et al. 2021) scaled by a factor of 2.4 to match the XMM analysis region to the γ -ray morphology at 1 TeV, the green points represent *Fermi*-LAT data in [0.4, 2.8] GeV (Li et al. 2021), the red points represent *Fermi*-LAT data in [30, 300] GeV (this work), the purple points represent VERITAS data in [0.5, 7.9] TeV (this work), the golden points represent HAWC data in [1.1, 246] TeV (this work), and the sky blue points represent LHAASO data in [10, 625] TeV (Cao et al. 2021, 2023). The green curves show the leptonic emission (synchrotron and inverse Compton) spectra produced by a PWN for different distance scenarios, the red curves show the hadronic emission (pion decay) produced by a SNR with a fixed SN energy 1.0×10^{51} erg for different distance scenarios assuming a gas density of 1 cm^{-3} , and the blue curves represent the combined (synchrotron + inverse Compton + pion decay) spectra.

HI data and the CO data show that the gas density in the region is at the level of $\sim 1 \text{ cm}^{-3}$.

To investigate the hadronic emission scenario in which the γ rays in [0.03, 625] TeV are produced by the pp collision with the ambient gas and the protons are accelerated by SNR G40.5-0.5, the hadronic γ -ray flux in the TeV regime is modeled by the NAIMA python package (Zabalza 2015) assuming a power-law proton injection spectrum,

$$f_p(E) = CE^{-\gamma} \exp(-E/E_c) \quad (14)$$

where E is the proton energy, γ is the power-law index, and E_c is an exponential cutoff. The best-fit result for the γ -ray spectrum at [0.03, 625] TeV gives a power-law index of $\gamma = 1.88 \pm 0.03$ and a cutoff energy of $E_c = 290 \pm 20$ TeV. The best-fit spectral index of 1.88 for the proton spectrum is harder than the spectral index of ~ 2.7 derived from the γ -ray observations of W44, Cas A, and IC443 (Acciari et al. 2009; Ack-

ermann et al. 2013). This SNR would also need to be located at a distance of ~ 1.5 kpc, which is incompatible with the distance estimation (5.5-8.5 kpc) for SNR G40.5-0.5, in order to produce the observed emission flux assuming the SN explosion energy of $\sim 10^{51}$ erg, an energy conversion efficiency of 10%, and the ambient gas density of $\sim 1 \text{ cm}^{-3}$. It should be noted that much higher gas density estimations were provided in the previous study by Duvidovich et al. (2020) by identifying individual clouds at different velocities near SNR G40.5-0.5. However, by calculating the γ -ray flux from the region enclosed by SNR G40.5-0.5 shell, it is found that SNR G40.5-0.5 region only emits $\sim 10\%$ of the total emission from MGRO J1908+06 in the energy range of the VERITAS data and cannot explain the majority of the extended MGRO J1908+06 emission at TeV energies.

In addition to the TeV emission of MGRO J1908+06 at [0.03, 625] TeV, the GeV emission at [0.4, 2.8] GeV

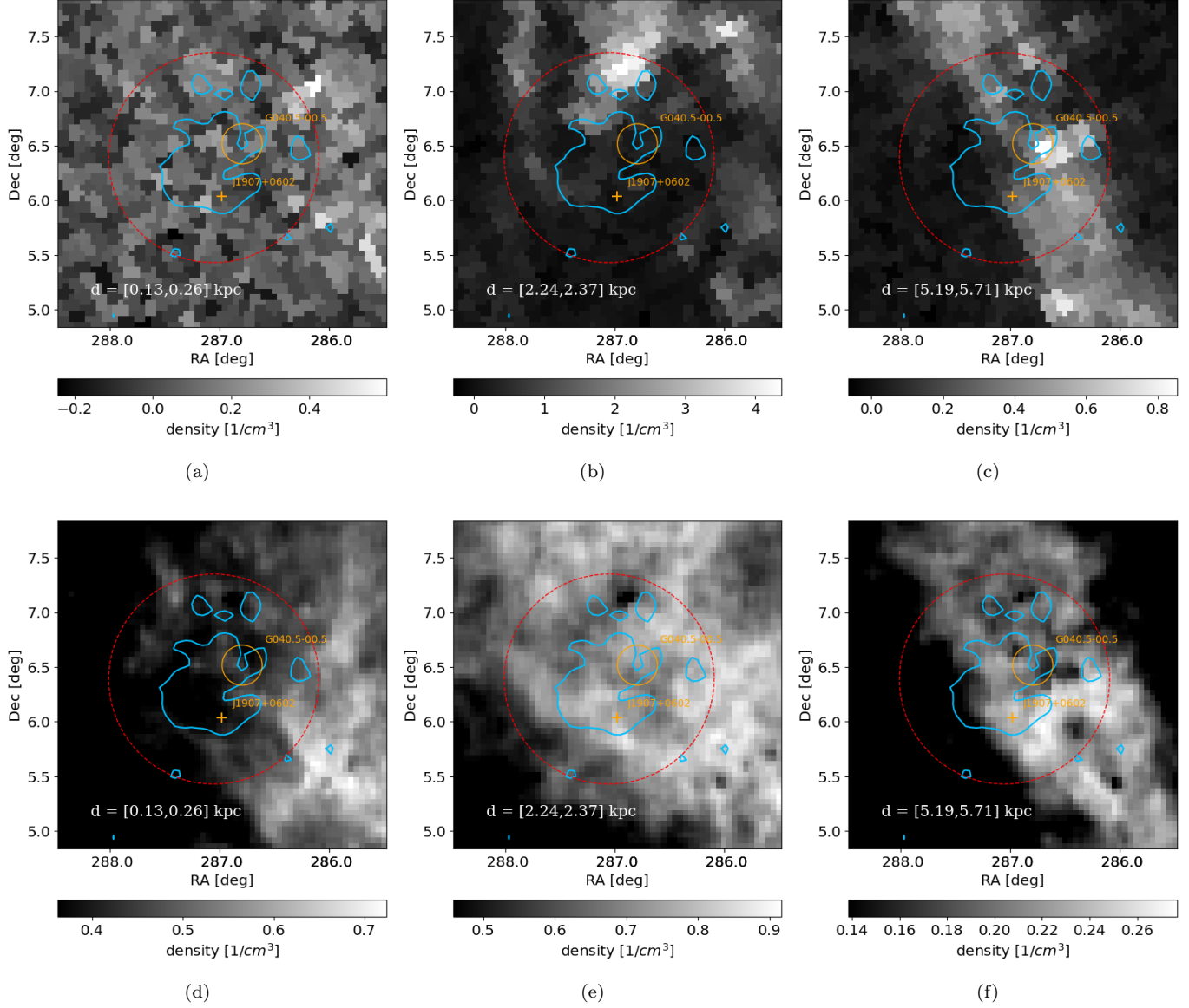


Figure 7. The maps of molecular gas density (top row) and atomic gas density (bottom row) in three distance intervals: 0.13-0.26 kpc (a,d), 2.24-2.37 kpc (b,e), and 5.19-5.71 kpc (c,f). The red dashed circular region is centered at the TeV emission centroid (RA, Dec) = (287.05°, 6.39°) with a radius of 0.96° containing 95% of the TeV emission. The skyblue contour shows the γ -ray morphology with $> 2.5\sigma$ significance in the VERITAS data. The orange cross indicates the location of PSR J1907+0602, and the orange circle outlines the shell size of the SNR G40.5-0.5. The coordinates are in J2000 equatorial degrees.

in the region of MGRO J1908+06 (labeled by the green points in Figure 6) discovered by Li et al. (2021) is also briefly summarized here. The best-fit to the GeV emission gives a softer power-law index of $\gamma = 2.81 \pm 0.12$. The soft GeV γ -ray spectra from SNRs have been argued to be caused by insufficient turbulence driving ahead of the shock (Brose et al. 2020), resulting in an energy-dependent diffusion coefficient. Li et al. (2021) associated the GeV emission to the possible interaction between cosmic rays and molecular clouds. Such a scenario

is supported by the average gas density of $\sim 45 \text{ cm}^{-3}$ in the GeV emission region at $\sim 8 \text{ kpc}$ Li et al. (2021).

5.3. A composite SNR/PWN model

One could consider a scenario in which the GeV emission ([0.4, 2.8] GeV) and the TeV emission ([0.03, 625] TeV) are produced by the same SNR/PWN system. In a such scenario, the [0.03, 625] TeV emission is produced by the PWN through IC scattering, while the [0.4, 2.8] GeV emission is produced by the SNR through pp collisions and subsequent pion decays. Such a model could

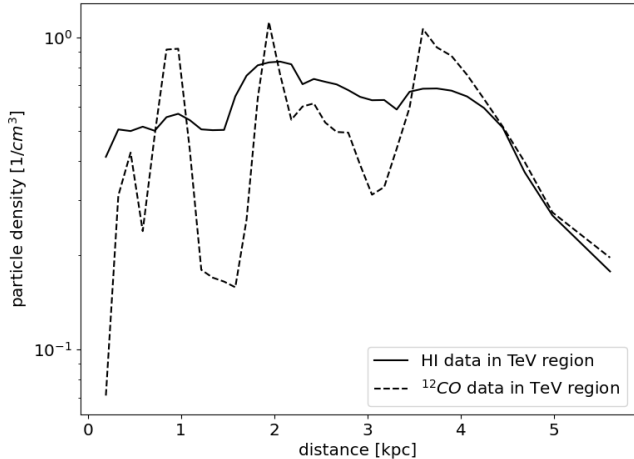


Figure 8. The ambient gas density as a function of distance. The dashed curve shows the density estimated using the CO data. The solid curve shows the density estimated using the HI data. The densities are measured from the TeV-emission region indicated by the red dashed circle in Figure 7).

exist without violating the scaled XMM upper limit if the SNR/PWN system is located at ~ 1.0 kpc with an age of ~ 6.0 kyr. The energy stored in protons above 1 GeV is $W_p = 1.0 \times 10^{50}$ erg for a low gas density of 1 cm^{-3} in the region. The energy stored in electrons above 1 GeV is $W_e = 1.5 \times 10^{47}$ erg, and the magnetic field $B = 10.7 \pm 6.6 \mu\text{G}$. The spectrum of the composite model corresponds to the dashed red curve (hadronic) and the dashed blue curve (hadronic + leptonic) in Figure 6.

6. DISCUSSION

Based on the observed γ -ray spectrum and morphology in *Fermi*-LAT, VERITAS, and HAWC data, and the estimations provided in Section 5, the possible scenarios for MGRO J1908+06 emission are discussed here.

A PWN at early times freely expands until it is crushed by the SNR reverse shock. The reverse shock disrupts the PWN and often results in an asymmetric morphology of the nebula due to an asymmetric reverse shock, generated by an inhomogeneous medium. The reverse shock compresses the PWN, eventually enabling the pulsar to exit the nebula. The separation between the PWN and the pulsar may also be driven by the pulsar’s velocity. See Blondin et al. (2001); Gelfand et al. (2009); Sudoh et al. (2019); Giacinti et al. (2020) for a discussion on the evolution of PWNe. When the pulsar exits the PWN, the confined PWN electrons continue to lose energy via radiative and adiabatic cooling, forming a relic nebula consisting of low-energy (below the cooling-break) electrons that have a cooling time

longer than the age of the system. A new PWN made up of freshly injected electrons forms near the pulsar which emits high-energy (above cooling-break) photons and have a shorter cooling time than the system age.

A leptonic PWN emission is favored to explain the TeV γ -ray emission, which is supported by the energy-dependent morphology shown in Figure 2: the emission with energies above the cooling break in γ -ray energy (~ 1.5 TeV) is concentrated around the pulsar, while the emission below the cooling-break energy has a larger offset from the pulsar. The separations between the γ -ray emission centroid and the location of the pulsar PSR J1907+0602 measured by the MW instruments are summarized in Table 4. The morphology of the γ -ray emission might be interpreted as a PWN undergoing an interaction with the SNR reverse shock. The true age of the system is 22 ± 9 kyr, and the magnetic field is $5.4 \pm 0.8 \mu\text{G}$, assuming the distance to the pulsar is 3.2 kpc. The reverse shock interaction and the motion of the pulsar could result in the separation between the relic PWN and the pulsar, creating asymmetric emission below the cooling break ($E_\gamma < 1.5$ TeV) with an offset from the location of the pulsar. At higher energies ($E_\gamma > 1.5$ TeV), the photons are created by high-energy electrons. These high-energy electrons with short cooling time are freshly produced by the pulsar, which result in more concentrated γ -ray emission around the pulsar.

The physical distance between the Gaussian centroid of *Fermi*-LAT emission reported in Table 1 and the location of PSR J1907+0602 is 19 pc, if one assumes a distance of 3.2 kpc to the pulsar. This distance implies a proper motion of ~ 845 km/s for the estimated age of 22 kyr, which is quite large compared to the mean 3-D pulsar birth velocity of 400 ± 265 km/s measured by a statistical study of 233 pulsar proper motions (Hobbs et al. 2005). However, it should be noted that the asymmetric γ -ray morphology could be a result of the quenching of the PWN by the reverse shock in addition to the motion of the progenitor star.

Although there is a lack of evidence for the connection between the GeV emission and the TeV emission, a composite system of the PWN of PSR J1907+0602 and the host SNR might explain both the emission in [0.4, 2.8] GeV and in [0.03, 625] TeV. This composite system should be ~ 6 kyr old and located at ~ 1 kpc in order to satisfy the XMM upper limit for the synchrotron emission, maintain a typical SN energy of $\sim 10^{51}$ erg. The distance estimation for PSR J1907+0602 is 3.2 kpc and has a nominal error of 20% (0.6 kpc, Abdo et al. 2010). The estimated distance ~ 1 kpc for the composite system is about four times the standard deviation from the nominal estimation.

Instrument	Energy range	R.A. (°)	Dec. (°)	r (°)	Δ (°)
<i>Fermi</i> -LAT	30 GeV - 2 TeV	286.99 ± 0.11	6.38 ± 0.11	0.6 ± 0.1	0.34 ± 0.11
VERITAS	0.5 TeV - 2.0 TeV	287.04 ± 0.01	6.33 ± 0.01	0.46 ± 0.01	0.30 ± 0.01
VERITAS	2.0 TeV - 7.9 TeV	287.00 ± 0.02	6.27 ± 0.02	0.42 ± 0.02	0.23 ± 0.02
HAWC	1 TeV - 3.16 TeV	287.02 ± 0.05	6.30 ± 0.05	0.53 ± 0.05	0.26 ± 0.07
HAWC	10 TeV - 31.6 TeV	287.05 ± 0.03	6.24 ± 0.03	0.45 ± 0.02	0.21 ± 0.04
HAWC	100 TeV - 316 TeV	287.02 ± 0.02	6.20 ± 0.04	0.40 ± 0.06	0.16 ± 0.04
PSR J1907+0602	–	286.98	6.04	–	–

Table 4. Summary of the best-fit Gaussian centroid and radius r , and the angular distance Δ to PSR J1907+0602 measured by the MW GeV-TeV instruments.

7. CONCLUSION

This paper presents the morphology and spectrum of MGRO J1908+06 using multi-wavelength observations across the GeV-TeV band. The multi-wavelength spectrum and morphology show a clear feature of an energy break at $E_\gamma \sim 1.5$ TeV. The energy break might be due to synchrotron cooling, which separates the cooled and uncooled particle populations. The multi-wavelength morphology shows that the MGRO J1908+06 emission has an energy dependence, revealing the distribution of particles at different energies. The *Fermi*-LAT and VERITAS data below the energy break reflect a relic PWN of low-energy electrons, while the VERITAS and HAWC data above the energy break reflect a new PWN of high-energy electrons.

The energy-dependent γ -ray morphology study of the MGRO J1908+06 TeV emission favors a leptonic PWN emission model. If the PWN is located at $d = 3.2 \pm 0.6$ kpc based on the dispersion measure (Abdo et al. 2010), the best-fit SED gives a true age $T = 22 \pm 9$ kyr and a magnetic field $B = 5.4 \pm 0.8 \mu\text{G}$. It is also interesting to note that if the TeV and GeV emission are produced by the same SNR/PWN composite system, such a system could exist at $d \sim 1$ kpc, $T \sim 6$ kyr, and $B \sim 10.7 \mu\text{G}$.

The synchrotron spectrum predicted from the estimated PWN parameters of PSR J1907+0602 will need new observations from the radio to MeV to verify. Future MeV instruments will be essential for revealing the complete hadronic emission in the MeV-GeV band and the connection between the GeV and TeV emission of MGRO J1908+06.

This publication utilizes data from Galactic ALFA HI (GALFA HI) survey data set obtained with the Arecibo L-band Feed Array (ALFA) on the Arecibo 305m telescope. The Arecibo Observatory is operated by SRI International under a cooperative agreement with the National Science Foundation (AST-1100968), and in alliance with Ana G. Méndez-Universidad Metropolitana, and the Universities Space Research Association. The GALFA HI surveys have been funded by the NSF through grants to Columbia University, the University of Wisconsin, and the University of California.

This research is supported by grants from the U.S. Department of Energy Office of Science, the U.S. National Science Foundation and the Smithsonian Institution, by NSERC in Canada, and by the Helmholtz Association in Germany. This research used resources provided by the Open Science Grid, which is supported by the National Science Foundation and the U.S. Department of Energy’s Office of Science, and resources of the National Energy Research Scientific Computing Center (NERSC), a U.S. Department of Energy Office of Science User Facility operated under Contract No. DE-AC02-05CH11231. We acknowledge the excellent work of the technical support staff at the Fred Lawrence Whipple Observatory and at the collaborating institutions in the construction and operation of the instrument. R.S. thanks NSF for support under NSF grants PHY-1913798 at UCLA and PHY-2110497 at Barnard College. The authors thank J. Gelfand and K. Mori for their constructive comments.

The HAWC collaboration acknowledges the support from: the US National Science Foundation (NSF); the US Department of Energy Office of High-Energy Physics; the Laboratory Directed Research and Development (LDRD) program of Los Alamos National Laboratory; Consejo Nacional de Ciencia y Tecnología (CONACyT), México, grants 271051, 232656, 260378, 179588, 254964, 258865, 243290, 132197, A1-S-46288, A1-S-22784, CF-2023-I-645, cátedras 873, 1563, 341, 323, Red HAWC, México; DGAPA-UNAM grants IG101323, IN111716-3, IN111419, IA102019, IN106521, IN110621,

IN110521 , IN102223; VIEP-BUAP; PIFI 2012, 2013, PROFOCIE 2014, 2015; the University of Wisconsin Alumni Research Foundation; the Institute of Geophysics, Planetary Physics, and Signatures at Los Alamos National Laboratory; Polish Science Centre grant, DEC-2017/27/B/ST9/02272; Coordinación de la Investigación Científica de la Universidad Michoacana; Royal Society - Newton Advanced Fellowship 180385; Generalitat Valenciana, grant CIDEGENT/2018/034; The Program Management Unit for Human Resources & Institutional Development, Research and Innovation, NXPO (grant number B16F630069); Coordinación General Académica e Innovación (CGAI-UdeG), PRODEP-SEP UDG-CA-499; Institute of Cosmic Ray Research (ICRR), University of Tokyo. H.F. acknowledges support by NASA under award number 80GSFC21M0002. We also acknowledge the significant contributions over many years of Stefan Westerhoff, Gaurang Yodh and Arnulfo Zepeda Dominguez, all deceased members of the HAWC collaboration. Thanks to Scott Delay, Luciano Díaz and Eduardo Murrieta for technical support.

The *Fermi*-LAT Collaboration acknowledges generous ongoing support from a number of agencies and institutes that have supported both the development and the operation of the LAT as well as scientific data

analysis. These include the National Aeronautics and Space Administration and the Department of Energy in the United States, the Commissariat à l’Energie Atomique and the Centre National de la Recherche Scientifique / Institut National de Physique Nucléaire et de Physique des Particules in France, the Agenzia Spaziale Italiana and the Istituto Nazionale di Fisica Nucleare in Italy, the Ministry of Education, Culture, Sports, Science and Technology (MEXT), High Energy Accelerator Research Organization (KEK) and Japan Aerospace Exploration Agency (JAXA) in Japan, and the K. A. Wallenberg Foundation, the Swedish Research Council and the Swedish National Space Board in Sweden. Additional support for science analysis during the operations phase is gratefully acknowledged from the Istituto Nazionale di Astrofisica in Italy and the Centre National d’Études Spatiales in France. This work performed in part under DOE Contract DE-AC02-76SF00515.

Software: FermiPy (v.1.2.0 Wood et al. 2017), FermiTools: Fermi Science Tools (v2.2.11 Fermi Science Support Development Team 2019), Eventdisplay (v.490 Maier & Holder 2017), NAIMA (v.0.10.0 Zabalza 2015), Gammapy (v.1.0 Acero et al. 2022)

APPENDIX

A. *FERMI*-LAT DATA ANALYSIS DETAILS

We perform a binned likelihood analysis with the latest FermiTools and FermiPy Python 3 packages, utilizing the `P8R3_SOURCE_V3` instrument response function (IRF) and account for energy dispersion, to perform data reduction and analysis. We organize the events by PSF type using `evtype=4,8,16,32` to represent the PSF0, PSF1, PSF2, and PSF3 components. A binned likelihood analysis is performed on each event type and then combined into a global likelihood function for the region of interest (ROI) to represent all events². We fit the square 10° ROI centered on the PWN position in equatorial coordinates using a pixel bin size 0.05° and 10 bins per decade in energy (19 total bins). The γ -ray sky for the ROI is modeled from the latest comprehensive *Fermi*-LAT source catalog based on 12 years of data, 4FGL (data release 3 (DR3), Abdollahi et al. 2022) for point and extended sources³ that are within 15° of the ROI center, as well as the latest Galactic diffuse and isotropic diffuse templates (`gll_iem_v07.fits` and `iso_P8R3_SOURCE_V3_v1.txt`, respectively)⁴.

With the source model described above, we allow the background components and sources with distances from the ROI center (chosen to be the PSR J1907+0602 position) $\leq 3.0^\circ$ to vary in spectral index and normalization. The test statistic (TS) value quantifies the significance for a source detection with a given set of location and spectral parameters. The significance of such a detection is proportional to the square root of the TS value (Mattox et al. 1996). The TS value is defined to be the natural logarithm of the ratio of the likelihood of one hypothesis (e.g. presence of one additional source) and the likelihood for the null hypothesis (e.g. absence of source):

$$TS = 2 \times \ln \left(\frac{\mathcal{L}_1}{\mathcal{L}_0} \right), \quad (\text{A1})$$

² See FermiPy documentation for details: <https://fermipy.readthedocs.io/en/0.6.8/config.html>

³ https://fermi.gsfc.nasa.gov/ssc/data/access/lat/12yr_catalog/.

⁴ LAT background models and appropriate instrument response functions: <https://fermi.gsfc.nasa.gov/ssc/data/access/lat/BackgroundModels.html>.

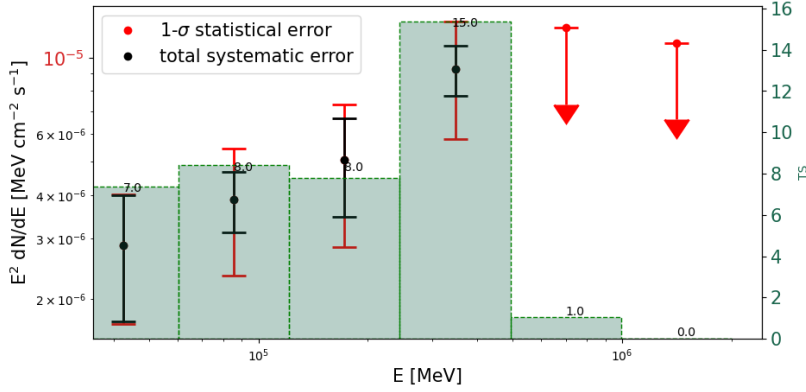


Figure 9. The Fermi-LAT SED flux data between 30 GeV to 2 TeV including statistical and systematic errors. The upper limits are plotted at the 95% confidence level. The green histogram displays the TS value for each energy bin.

TS values > 25 correspond to a detection significance $> 4\sigma$ for 4 degrees of freedom (DOF).

A.1. *Fermi-LAT Systematic Effect Study*

We account for systematic uncertainties introduced by the choice of the interstellar emission model (IEM) and the IRFs, which mainly affect the spectrum of the measured γ -ray emission. We have followed the prescription developed in de Palma et al. (2013); Acero et al. (2016), based on generating eight alternative IEMs using a different approach than the standard IEM (see Acero et al. 2016, for details). For this analysis, we employ the eight alternative IEMs (aIEMs) that were generated for use on Pass 8 data in the *Fermi* Galactic Extended Source Catalog (FGES, Ackermann et al. 2017). The extended γ -ray source coincident with MGRO J1908+06 is refit with each aIEM to obtain a set of eight values for the spectral flux that we compare to the standard model following equation (5) in Acero et al. (2016). We estimate the systematic uncertainties from the effective area⁵ while enabling energy dispersion. For energies between 30 GeV and 100 GeV, the uncertainty from the effective area is $\pm 3\%$. Beyond 100 GeV, the uncertainty from the effective area increases as: $\pm(3\% + 12\% \times (\log(\frac{E}{\text{MeV}}) - 5))$. The IEM and IRF systematic errors are taken to be independent of each other, so we combine the values using the quadratic sum to represent the total systematic error. We find that the total systematic error is comparable to the statistical error, primarily from the increasing uncertainty on the effective area with energy. The 1σ statistical uncertainty remains the largest source of error, however, so we only include statistical errors in this report. Figure 9 displays both statistical and systematic errors for reference.

B. VERITAS DATA ANALYSIS DETAILS

B.1. *Low-rank Perturbation Method*

The Low-rank Perturbation Method (LPM) is the primary analysis method for background prediction used in this paper. The LPM predicts the background for γ -ray-like events using the event distribution in the cosmic-ray-like region in the parameter space of mean reduced scaled length ($MSCL$) and mean reduced scaled width ($MSCW$). The mean reduced scaled length ($MSCL$) is defined as

$$MSCL = \frac{1}{N} \sum_{i=1}^N \frac{l_{\text{obs},i}(s, R) - \bar{l}_{\text{sim}}(s, R)}{\sigma_{l,\text{sim}}(s, R)} \quad (\text{B2})$$

, and the mean reduced scaled width ($MSCW$) is defined as

$$MSCW = \frac{1}{N} \sum_{i=1}^N \frac{w_{\text{obs},i}(s, R) - \bar{w}_{\text{sim}}(s, R)}{\sigma_{w,\text{sim}}(s, R)}, \quad (\text{B3})$$

where N is the number of telescopes with images passing selection cuts, $l_{\text{obs},i}$ ($w_{\text{obs},i}$) is the shower length (width) observed by the i th telescope, \bar{l}_{sim} (\bar{w}_{sim}) is the expected length (width) of the simulated events, and $\sigma_{l,\text{sim}}$ ($\sigma_{w,\text{sim}}$)

⁵ https://fermi.gsfc.nasa.gov/ssc/data/analysis/scitools/Aeff_Systematics.html

is the 90 % containment variation of the length and width of the simulated events. The length and the width of the shower are binned in shower size s (the summation of the charge of all the pixels of the image) and impact parameter R (the distance from the telescope to the shower axis).

The events passing the mean reduced scaled parameters cuts ($MSCL < 0.6$ and $MSCW < 0.6$) are the γ -ray-like events, and the events failing the mean reduced scaled parameters cuts are the cosmic-ray-like events. The event distribution in the binned $MSCL - MSCW$ space are the "matrix", in which the matrix element M_{ij} is the count of the events in the bin with index i labeling the $MSCL$ dimension and j the $MSCW$ dimension.

An OFF matrix M^{OFF} is assembled from a set of γ -ray-free archival observations with observing zenith and azimuth angles matching the ON observation matrix M^{ON} . The LPM method predicts the difference $\delta M_{ij} = M^{\text{ON}} - M^{\text{OFF}}$ in the γ -like region by assuming that M_{ON} is a low rank matrix and minimizing the Frobenius norm $\|M^{\text{ON}} - M^{\text{OFF}} - \delta M\|_F$ in the cosmic-ray-like region.

The procedure of the method is following. Given an OFF-run matrix M^{OFF} , the Singular Value Decomposition (SVD) is

$$M^{\text{OFF}} = \sum_k \sigma_k^{\text{OFF}} \vec{u}_k^{\text{OFF}} \vec{v}_k^{\text{OFF}}, \quad (\text{B4})$$

where M^{OFF} is the γ -ray-free matrix constructed from the OFF runs that match the ON runs in observing conditions and is normalized to the cosmic-ray-like region of the M^{ON} , i.e.

$$\sum_{ij \in \text{CR-like}} M_{ij}^{\text{ON}} = \sum_{ij \in \text{CR-like}} M_{ij}^{\text{OFF}}. \quad (\text{B5})$$

A linear perturbation theory can be built around M^{OFF} to the approximation of background matrix \tilde{M}^{ON} of the ON runs, i.e.

$$\tilde{M}_{ij}^{\text{ON}} = \sum_k \sigma_k^{\text{ON}} \vec{u}_k^{\text{ON}} \vec{v}_k^{\text{ON}} \approx M_{ij}^{\text{OFF}} + \delta M_{ij} \quad (\text{B6})$$

where $\delta M_{ij} = \sum_{k,n=1}^d u_i^{(k)} v_j^{(n)} t_{kn}$ is the matrix perturbation based on the eigenvectors of M^{OFF} , $u_i^{(k)}$ ($v_j^{(n)}$) is the entry in the eigenvector \vec{u}_k^{OFF} (\vec{v}_n^{OFF}), and the coefficient matrix t_{kn} is the solution that needs to be found.

To find t_{kn} , one can expand the perturbations around the singular values and the eigenvectors,

$$\sigma_k^{\text{ON}} = \sigma_k^{\text{OFF}} + \delta \sigma_k \quad (\text{B7})$$

$$\vec{u}_k^{\text{ON}} = \vec{u}_k^{\text{OFF}} + \delta \vec{u}_k \quad (\text{B8})$$

$$\vec{v}_k^{\text{ON}} = \vec{v}_k^{\text{OFF}} + \delta \vec{v}_k \quad (\text{B9})$$

The perturbations, $\delta \vec{u}_k$ and $\delta \vec{v}_k$, can be written as the linear combinations of the M^{OFF} basis, i.e.

$$\delta \vec{u}_k = \sum_{n=1}^d C_{kn} \vec{u}_n^{\text{OFF}} \quad (\text{B10})$$

$$\delta \vec{v}_k = \sum_{n=1}^d D_{kn} \vec{v}_n^{\text{OFF}} \quad (\text{B11})$$

, where d is the number of dominant singular values. Note that the coefficients need to satisfy $C_{kn} = -C_{nk}$ and $D_{kn} = -D_{nk}$ for U and V matrices to be unitary.

Substitute Equation B7 B8 B9 with $\sum_k \sigma_k^{\text{ON}} \vec{u}_k^{\text{ON}} \vec{v}_k^{\text{ON}}$ in Equation B6, one can find that, to the first-order approximation, the perturbation is

$$\delta M_{ij} = \sum_{k,n=1}^d u_i^{(k)} v_j^{(n)} \underbrace{[\delta_{kn} \delta \sigma_k + \sigma_n C_{kn} - \sigma_k D_{kn}]}_{t_{kn}} \quad (\text{B12})$$

where δ_{kn} is Kronecker delta function.

The matrix t , which contains the perturbations, can be solved by minimizing the regularized Frobenius norm in the CR-like region,

$$\text{Minimize} \left(\sum_{ij \in \text{CR-like}} \Delta_{ij}^2 + \beta \sum_k^{k=d} t_{kk}^2 \right) \quad (\text{B13})$$

where $\Delta_{ij} = \tilde{M}_{ij}^{\text{ON}} - M_{ij}^{\text{OFF}} - \delta M_{ij} = \Delta M_{ij} - \delta M_{ij}$, t_{kk} are the perturbations on the singular values, and β is the regularization parameter to be optimized. The solution to the minimization above can be found by vectorizing Equation B12, which rearranges the matrices into single-column vectors, i.e. $t_{kn} \rightarrow t_y$ and $\Delta M_{ij} \rightarrow \Delta M_x$, and Equation B12 becomes

$$\Delta \vec{M} = A \vec{t}, \quad (\text{B14})$$

where the products of $u_i^{(k)} v_j^{(n)}$ and the regularization constant β form the element A_{xy} , i.e.

$$A = \begin{bmatrix} u_0^{(0)} v_0^{(0)} & u_0^{(0)} v_0^{(1)} & \dots & u_0^{(k)} v_0^{(k)} & \dots & u_0^{(k)} v_0^{(n)} & \dots \\ u_0^{(0)} v_1^{(0)} & u_0^{(0)} v_1^{(1)} & \dots & u_0^{(k)} v_1^{(k)} & \dots & u_0^{(k)} v_1^{(n)} & \dots \\ \vdots & \vdots & & \vdots & & \vdots & \\ u_i^{(0)} v_j^{(0)} & u_i^{(0)} v_j^{(1)} & \dots & u_i^{(k)} v_j^{(k)} & \dots & u_i^{(k)} v_j^{(n)} & \dots \\ \vdots & \vdots & & \vdots & & \vdots & \\ \beta & 0 & & 0 & & 0 & \\ \vdots & \vdots & & \vdots & & \vdots & \\ 0 & 0 & & \beta & & 0 & \\ \vdots & \vdots & & \vdots & & \vdots & \end{bmatrix} \quad (\text{B15})$$

, and

$$\Delta \vec{M}^\top = \left[\Delta M_{00} \quad \Delta M_{01} \quad \dots \quad \Delta M_{ij} \quad \dots \quad 0 \quad \dots \quad 0 \quad \dots \right] \quad (\text{B16})$$

The least-square solution is found to be

$$\vec{t} = (A^\top W A)^{-1} A^\top W \Delta \vec{M}, \quad (\text{B17})$$

where

$$W_{x_1 x_2} = \begin{cases} \delta_{x_1 x_2} \sigma_{x_1}, & \text{if } x_{1,2} \in \text{CR-like} \\ 0, & \text{otherwise} \end{cases} \quad (\text{B18})$$

where $\sigma_x = 1/\sqrt{M_x^{\text{ON}}}$ is the statistical uncertainty of the matrix element.

The resulting perturbations, $\delta\sigma$, $\delta\vec{u}$ and $\delta\vec{v}$, predict the background normalization in the blinded γ -like region ($\sum_{ij \in \gamma\text{-like}} M_{ij}$). The optimization for the regularization parameter β , and binning of the matrices, as well as the dependence on the initial matrix selection, will be discussed in the future publication of the background method.

B.2. Validation of Background Estimation of VERITAS Data

To validate the background estimation for the extended source in the VERITAS analysis, five independent sets of γ -ray-free data are selected to mimic the ON data (observations of MGRO J1908+06). The mimic data runs are selected from extragalactic observations of point-like sources with events from the locations of the point-like sources excluded. The total exposure of a mimic data set is required to be more than 80% of the exposure of the ON observations. The telescope pointing coordinate (RA, Dec) of each mimic run is artificially changed to the pointing coordinate of the corresponding ON run to recreate a mimic sky map. The arrival coordinates of a shower event in the mimic data **are** also changed accordingly,

$$(\text{RA}, \text{Dec})_{\text{evt}} = (\text{RA}, \text{Dec})_{\text{ON}} + (X, Y)_{\text{derot}}, \quad (\text{B19})$$

where $(X, Y)_{\text{derot}}$ is the de-rotated (X, Y) coordinate of the mimic data event in the telescope camera frame.

The background estimations for the 5 mimic data sets are used as an estimation of the systematic uncertainty for the ON-data background. The systematic uncertainty of the background prediction is assessed by computing the root-mean-square of the relative residuals of the mimic data sets after subtracting the background, i.e.

$$\sigma_{\text{sys}}(x, y) = \sqrt{\frac{1}{5} \sum_{i=1}^5 \left(\frac{D_i(x, y) - B_i(x, y)}{D_i(x, y)} \right)^2}, \quad (\text{B20})$$

where $D_i(x, y)$ ($B_i(x, y)$) is the data (background) count in the sky map bin (x, y) in the mimic data set i .

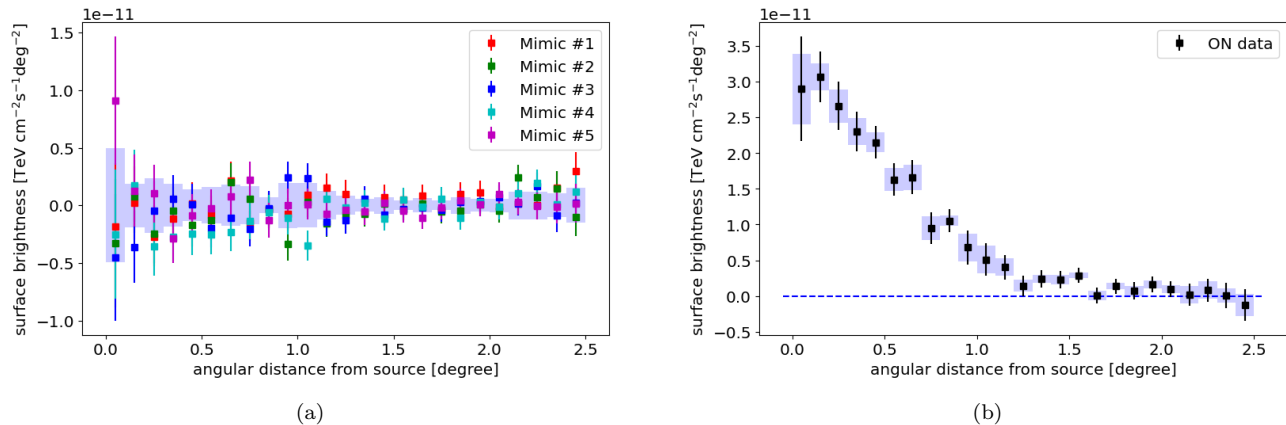


Figure 10. The radial profile of the residuals after background subtraction is shown in the unit of surface brightness for (a) the mimic data sets and (b) the ON data set. The vertical bars represent the data statistical uncertainties, while the blue envelopes are the estimated systematic uncertainties using the root-mean-square of the mimic data profiles.

Centered at the location of 3HWC J1908+063, Figure 10 (a) shows the radial profile of the residuals of the mimic data sets after background subtraction (using the background method described in Section B.1) in the unit of $E^2 dN/dE$ and the envelope of the residual RMS that represents the systematic uncertainty of background estimation. Figure 10 (b) shows the residuals of the ON data set after background subtraction with the envelope of systematic uncertainty derived from the mimic data.

B.3. Cross-check: Field-of-view (FoV) Background Method

The FoV Background estimation technique is used as a secondary background estimation method for the VERITAS analysis. This approach relies on the creation of background models from gamma-ray free data. The background models are generated from archival VERITAS data with quality cuts based on realistic analysis data selection cuts for different observing parameters (azimuth, elevation, gamma-hadron separation cut, epoch, night sky background).

During the background model generation, bright and extended gamma-ray sources are excluded and sources in the VERITAS catalogue are masked with a 0.3 degree radius. The background rate is calculated in a (RA, Dec) aligned coordinate system with dependence on energy, radius from the center of the camera, longitude and latitude. In this process the full-enclosure (i.e. offset dependent) instrument response functions are interpolated at the average observation parameters. In the analysis, observations are stacked onto a map with a bin size of 0.02 degree and a lower energy threshold of 0.8 TeV is used. A power-law-based correction is applied to the background rate with the norm and tilt allowed to float freely. Exclusion regions are placed around the HAWC source (1 degree), around the pulsars in the FoV (0.5 degree) and around the two first eastern (e1, e2) and western (w1, w2) jet emission regions of SS 433 (0.5 degree).

To estimate the systematics and biases in the background prediction, five mimic datasets are created that match the observations in terms of exposure, elevation, azimuth, night-sky-background and epoch as described in Section B.2. These files are analyzed with the same pipeline as the observational data.

The comparison between the cross-check provided by the Gammapy FoV method and the nominal spectral measurement provided by the LPM method is shown in Figure 11.

C. HAWC SYSTEMATIC UNCERTAINTIES

The detector performance and simulations produce a series of systematic uncertainties that are described in detail in Abeysekara et al. (2017) and Abeysekara et al. (2019b). The spectral and spatial parameters with positive and negative shifts are added in quadrature to account for the upward and downward uncertainties, respectively. These uncertainties are included in Table 3.

REFERENCES

Abdo, A., Ackermann, M., Ajello, M., et al. 2010, The Astrophysical Journal, 711, 64

Abdo, A., Ajello, M., Allafort, A., et al. 2013, The Astrophysical Journal Supplement Series, 208, 17

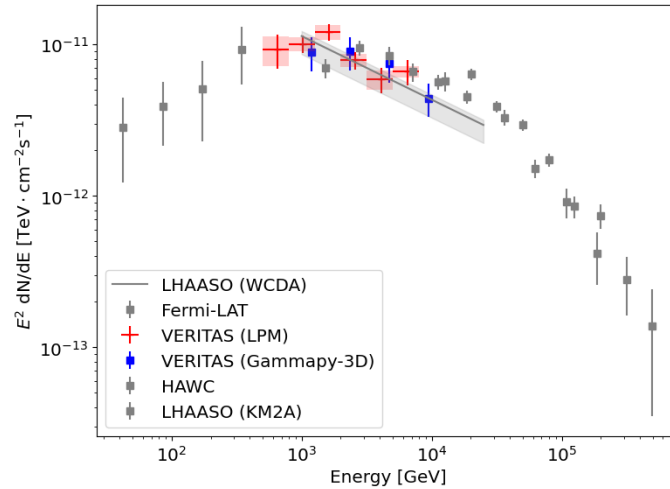


Figure 11. The cross-check VERITAS spectral measurement provided by the Gammamy FoV method (blue points) compared to the spectral measurement provided by the LPM method (red points).

- Abdo, A. A., Allen, B., Berley, D., et al. 2007, *The Astrophysical Journal*, 664, L91
- Abdo, A. A., Allen, B., Aune, T., et al. 2008, *ApJ*, 688, 1078, doi: [10.1086/592213](https://doi.org/10.1086/592213)
- Abdollahi, S., Acero, F., Ackermann, M., et al. 2020, *ApJS*, 247, 33, doi: [10.3847/1538-4365/ab6bcb](https://doi.org/10.3847/1538-4365/ab6bcb)
- Abdollahi, S., Acero, F., Baldini, L., et al. 2022, *ApJS*, 260, 53, doi: [10.3847/1538-4365/ac6751](https://doi.org/10.3847/1538-4365/ac6751)
- Abeysekara, A., Albert, A., Alfaro, R., et al. 2017, *Science*, 358, 911
- . 2018, *Nature*, 562, 82
- . 2020, *Physical review letters*, 124, 021102
- Abeysekara, A. U., Albert, A., Alfaro, R., et al. 2017, *ApJ*, 843, 39, doi: [10.3847/1538-4357/aa7555](https://doi.org/10.3847/1538-4357/aa7555)
- . 2018, *Nature*, 562, 82, doi: [10.1038/s41586-018-0565-5](https://doi.org/10.1038/s41586-018-0565-5)
- . 2019a, *ApJ*, 881, 134, doi: [10.3847/1538-4357/ab2f7d](https://doi.org/10.3847/1538-4357/ab2f7d)
- . 2019b, *ApJ*, 881, 134, doi: [10.3847/1538-4357/ab2f7d](https://doi.org/10.3847/1538-4357/ab2f7d)
- Abeysekara, A. U., et al. 2021, *PoS, ICRC2021*, 828, doi: [10.22323/1.395.0828](https://doi.org/10.22323/1.395.0828)
- Acciari, V., Aliu, E., Arlen, T., et al. 2009, *The Astrophysical Journal*, 698, L133
- Acero, F., Ackermann, M., Ajello, M., et al. 2016, *ApJS*, 224, 8, doi: [10.3847/0067-0049/224/1/8](https://doi.org/10.3847/0067-0049/224/1/8)
- Acero, F., Aguasca-Cabot, A., Buchner, J., et al. 2022, *Gammamy: Python toolbox for gamma-ray astronomy*, Zenodo, doi: [10.5281/zenodo.7311399](https://doi.org/10.5281/zenodo.7311399)
- Ackermann, M., Ajello, M., Allafort, A., et al. 2013, *Science*, 339, 807
- Ackermann, M., Ajello, M., Baldini, L., et al. 2017, *ApJ*, 843, 139, doi: [10.3847/1538-4357/aa775a](https://doi.org/10.3847/1538-4357/aa775a)
- Aharonian, F., Atoyan, A., & Voelk, H. 1995, *Astronomy and Astrophysics*, 294, L41
- Aharonian, F., Akhperjanian, A., Anton, G., et al. 2009, *Astronomy & Astrophysics*, 499, 723
- Albert, A., Alfaro, R., Alvarez, C., et al. 2022, *The Astrophysical Journal*, 928, 116
- Albert, A., Alfaro, R., Alvarez, C., et al. 2024, arXiv e-prints, arXiv:2405.06050, doi: [10.48550/arXiv.2405.06050](https://doi.org/10.48550/arXiv.2405.06050)
- Aliu, E., Archambault, S., Aune, T., et al. 2014, *The Astrophysical Journal*, 787, 166
- Atwood, W., Albert, A., Baldini, L., et al. 2013, arXiv e-prints, arXiv:1303.3514, <https://arxiv.org/abs/1303.3514>
- Atwood, W. B., Abdo, A. A., Ackermann, M., et al. 2009, *ApJ*, 697, 1071, doi: [10.1088/0004-637X/697/2/1071](https://doi.org/10.1088/0004-637X/697/2/1071)
- Bartoli, B., Bernardini, P., Bi, X., et al. 2012, *The Astrophysical Journal*, 760, 110
- Bhattacharjee, P., Chaudhury, S., & Kundu, S. 2014, *The Astrophysical Journal*, 785, 63
- Blondin, J. M., Chevalier, R. A., & Frierson, D. M. 2001, *The Astrophysical Journal*, 563, 806
- Bolatto, A. D., Wolfire, M., & Leroy, A. K. 2013, *Annual Review of Astronomy and Astrophysics*, 51, 207
- Breuhaus, M., Hahn, J., Romoli, C., et al. 2021, *The Astrophysical Journal Letters*, 908, L49
- Brose, R., Pohl, M., Sushch, I., Petruk, O., & Kuzyo, T. 2020, *Astronomy & Astrophysics*, 634, A59
- Bruel, P., Burnett, T. H., Digel, S. W., et al. 2018, arXiv e-prints, arXiv:1810.11394, <https://arxiv.org/abs/1810.11394>
- Bucciantini, N., Bandiera, R., Blondin, J., Amato, E., & Del Zanna, L. 2004, *Astronomy & Astrophysics*, 422, 609
- Büsching, I., De Jager, O., Potgieter, M., & Venter, C. 2008, *The Astrophysical Journal*, 678, L39

- Cao, Z., Aharonian, F., An, Q., et al. 2021, *Nature*, 594, 33
— . 2023, arXiv preprint arXiv:2305.17030
- Crestan, S., Giuliani, A., Mereghetti, S., et al. 2021, *Monthly Notices of the Royal Astronomical Society*, 505, 2309
- Dame, T. M., Hartmann, D., & Thaddeus, P. 2001, *The Astrophysical Journal*, 547, 792
- de Palma, F., Brandt, T. J., Johannesson, G., & Tibaldo, L. 2013, arXiv e-prints, arXiv:1304.1395.
<https://arxiv.org/abs/1304.1395>
- De Sarkar, A., & Gupta, N. 2022, arXiv preprint arXiv:2205.01923
- Downes, A., Pauls, T., & Salter, C. 1980, *Astronomy and Astrophysics*, 92, 47
- Duvidovich, L., Petriella, A., & Giacani, E. 2020, *Monthly Notices of the Royal Astronomical Society*, 491, 5732
- Fermi Science Support Development Team. 2019, *Fermitools: Fermi Science Tools, Astrophysics Source Code Library*, record ascl:1905.011.
<http://ascl.net/1905.011>
- Gelfand, J. D., Slane, P. O., & Zhang, W. 2009, *The Astrophysical Journal*, 703, 2051
- Giacinti, G., Mitchell, A., López-Coto, R., et al. 2020, *Astronomy & Astrophysics*, 636, A113
- Hobbs, G., Lorimer, D., Lyne, A., & Kramer, M. 2005, *Monthly Notices of the Royal Astronomical Society*, 360, 974
- Kostunin, D., Mohrmann, L., Wilhelmi, E., et al. 2021, arXiv preprint arXiv:2108.03401
- Li, J., Liu, R.-Y., de Oña Wilhelmi, E., et al. 2021, *The Astrophysical Journal Letters*, 913, L33
- Lyne, A., Stappers, B., Bogdanov, S., et al. 2017, *The Astrophysical Journal*, 834, 137
- Maier, G., & Holder, J. 2017, arXiv preprint arXiv:1708.04048
- Mattox, J. R., Bertsch, D. L., Chiang, J., et al. 1996, *ApJ*, 461, 396, doi: [10.1086/177068](https://doi.org/10.1086/177068)
- Pandel, D., & Scott, R. 2012, *AIP Conference Proceedings*, 1505, 329
- Peek, J., Babler, B. L., Zheng, Y., et al. 2017, *The Astrophysical Journal Supplement Series*, 234, 2
- Porter, T. A., Johannesson, G., & Moskalenko, I. V. 2017, *The Astrophysical Journal*, 846, 67
- Sudoh, T., Linden, T., & Beacom, J. F. 2019, *Physical Review D*, 100, 043016
- Vianello, G., Lauer, R. J., Younk, P., et al. 2015, arXiv e-prints, arXiv:1507.08343.
<https://arxiv.org/abs/1507.08343>
- Weekes, T., Badran, H., Biller, S., et al. 2002, *Astroparticle Physics*, 17, 221
- Wood, M., Caputo, R., Charles, E., et al. 2017, in *International Cosmic Ray Conference*, Vol. 301, 35th International Cosmic Ray Conference (ICRC2017), 824.
<https://arxiv.org/abs/1707.09551>
- Yang, J., Zhang, J.-L., Cai, Z.-Y., Lu, D.-R., & Tan, Y.-H. 2006, *Chinese Journal of Astronomy and Astrophysics*, 6, 210
- Young, M. D., Chan, L. S., Burman, R. R., & Blair, D. G. 2010, *Monthly Notices of the Royal Astronomical Society*, 402, 1317
- Zabalza, V. 2015, *Proc. of International Cosmic Ray Conference 2015*, 922
- Zhou, H., Rho, C. D., Vianello, G., & HAWC Collaboration. 2017, in *International Cosmic Ray Conference*, Vol. 301, 35th International Cosmic Ray Conference (ICRC2017), 689, doi: [10.22323/1.301.0689](https://doi.org/10.22323/1.301.0689)